

1 **Influence of Upper Mantle Anisotropy on Isotropic**
2 **P-Wave Tomography Images Obtained in the Eastern**
3 **Mediterranean Region**

4 **Judith M. Confal¹, Maximiliano J. Bezada², Tuna Eken¹, Manuele Faccenda³,**
5 **Erdinc Saygin^{4,5}, Tuncay Taymaz¹**

6 ¹Department of Geophysical Engineering, The Faculty of Mines, Istanbul Technical University, Istanbul,
7 Turkey

8 ²Department of Earth Sciences, University of Minnesota-Twin Cities, Minneapolis, USA

9 ³Department of Geoscience, University of Padua, Padua, Italy

10 ⁴Deep Earth Imaging, Future Science Platform, CSIRO, Perth, Western Australia, Australia

11 ⁵School of Physics, Mathematics and Computing, University of Western Australia, Perth, Western
12 Australia, Australia

13 **Key Points:**

- 14 • Velocity perturbations show several tears and break-off areas in the Hellenic and
15 Cyprian slabs
- 16 • Main P-wave velocity perturbation features are similar in isotropic and anisotropy-
17 corrected models
- 18 • Discrepancies of up to $\pm 2\%$ between models highlight the importance of anisotropy
19 to resolve small structures

Corresponding author: Judith M. Confal, Department of Geophysical Engineering, The
Faculty of Mines, Istanbul Technical University, 34469 Maslak, Sariyer, Istanbul, Turkey,
judithconfal@gmail.com

Abstract

Seismic body-wave tomography studies typically assume an isotropic upper mantle, possibly mapping anisotropy into artificial isotropic velocity anomalies in the resulting images. The Eastern Mediterranean with its oceanic, continental, and extinct subduction systems, as well as dense station coverage, provides an ideal setting to explore this issue. To examine the influence of seismic anisotropy, our study deals with both synthetic and real data inversions in which realistic seismic anisotropy models derived from 3D mantle convection simulations and shear wave splitting measurements are taken as *a priori* constraints. Spatial large-scale velocity perturbations are mostly consistent between models derived with and without considering anisotropy. Small differences in the magnitude (up to 2%) and shape of velocity perturbations occur and some structures are less diffuse when including anisotropy. Additionally, good backazimuthal coverage of teleseismic events and a larger data set improve the resolution of our model with respect to previous tomography studies and allow us to better interpret first-order isotropic velocity anomalies. Key features, such as the half-arc subducting oceanic plate in the southern Aegean and a wide and deep tear in the slab beneath southwestern Turkey, are clearly visible in all models. Our final tomography images also provide evidence for a shallow horizontal tear in the northern Hellenides and a vertical tear between two parts of the Cyprian slab. In eastern Anatolia, slab-related high-velocity anomalies are absent due to the continental collision and break-off.

Plain Language Summary

Understanding current and prior mantle flow in the upper mantle is fundamental for the reconstruction of plate tectonics. P-wave tomography is used as a method to monitor seismic velocity changes at great depths. These anomalies give clues about various geodynamic events, for example, downgoing plates and upwelling mantle material. However, whenever mantle flow is involved, intrinsically anisotropic minerals tend to align in certain directions, which makes the velocities directionally dependent and hence could lead to distortion of the results. Therefore, it may be important to include directional parameters in the calculations, to achieve a better resolution and a more accurate knowledge of the subsurface. Considering the effect of seismic anisotropy is particularly important in the very tectonically active region of the Eastern Mediterranean. We found that by including seismic anisotropy, the magnitude and geometry of some anomalies change but spatially large anomalies do not change significantly. We were able to recover the shape of the slab in detail and found

52 evidence for break-offs and tears in western Greece and Turkey, nearby Cyprus and eastern
53 Turkey in all models.

54 **1 Introduction**

55 Seismic tomography is a well-established method that is frequently used to investigate upper
56 mantle subduction tectonics and kinematics by constraining variations in seismic velocity.
57 Over the last two decades, there have been many P and/or S wave tomography studies
58 conducted to understand the complex tectonic setting beneath the Eastern Mediterranean
59 region (e.g., Biryol et al., 2011; Blom et al., 2020; Çubuk-Sabuncu et al., 2017; Fichtner,
60 Saygin, et al., 2013; Fichtner, Trampert, et al., 2013; Piromallo & Morelli, 2003; Portner
61 et al., 2018) (Figure 1). Although these studies employed different data sets, the resolved
62 images of the lithosphere and asthenosphere have implied very similar features in the man-
63 tle such as subducting and fragmented slabs as well as hot upwelling material. However,
64 it is noted that some anomalies, for instance, those underneath the slab or small velocity
65 perturbations, are often left out from interpretations, which mostly focus on the large-scale
66 characteristics of seismic velocity anomalies.

67 In the Eastern Mediterranean region, the Hellenic (Aegean) subduction zone, which accom-
68 modates the convergent plate motion between the Nubian and Eurasian plates, has been
69 active since the Eocene (e.g., Jolivet et al., 2015) and has produced present-day seismic
70 anisotropy in various directions and strengths. Confal et al. (2018) numerically simulated
71 the strain-induced lattice preferred orientations (LPO) of A-type olivine in the upper mantle
72 for a hypothetical subduction zone resembling the Hellenic subduction system. The mod-
73 eling results are consistent with observations on seismic anisotropy, i.e., station averaged
74 fast polarization directions (FPDs) primarily based on shear wave splitting (SWS) measure-
75 ments, which indicate the presence of strong anisotropy evidenced by splitting time delays
76 (TDs) of up to 2 s (e.g., Confal et al., 2016; Evangelidis et al., 2011; Paul et al., 2014). These
77 measured time delays between fast and slow shear waves are proportional to the thickness of
78 the anisotropic layer and the strength of the anisotropy. For teleseismic isotropic tomogra-
79 phy studies with incoming waves that have steep incidence angles, the propagation direction
80 would be subparallel to the anisotropic slow direction in layers with horizontally aligned fast
81 and intermediate directions. Consequently, this produces delayed arrival times that can be
82 mapped by isotropic tomography into a low-velocity anomaly as shown by Bezada et al.
83 (2016). Conversely, mantle structures with vertically aligned fabrics would produce high-

84 velocity perturbations (Figure 2). Seismic velocity perturbations of up to $\pm 3\text{-}4\%$ in various
85 tomographic studies (e.g., P and S waves and surface waves) are, in general, attributed to
86 the lateral variations in temperature and partial melt, or the composition of crustal and
87 mantle rocks. Velocity anomalies caused by anisotropy could interfere with real isotropic
88 velocity anomalies and lead to incorrect interpretations of the thermophysical parameters.
89 Sobolev et al. (1999) used synthetic data to show that in isotropic P-wave tomography,
90 significant artifacts can occur for some specific anisotropy structures, especially in regions
91 with a dipping olivine a-axis. Lloyd and van der Lee (2008) examined the influence of
92 anisotropy on both S- and Rayleigh wave derived isotropic tomographic images obtained for
93 North America. They were able to quantify the anisotropic bias in images and concluded
94 that the magnitude of the bias decreased with increasing depth location of the anisotropic
95 material. Eakin et al. (2010) also observed a correlation between low-velocity anomalies
96 within the tomography model and large splitting time delays in the Cascadian subduction
97 region. O’Driscoll et al. (2011) applied anisotropic time corrections to P-wave traveltimes
98 residuals that were calculated based on SKS splitting parameters for the western United
99 States. Their results highlighted the importance of the magnitude of anisotropy rather than
100 its orientation, under the assumption that the axis of symmetry is horizontal. Furthermore,
101 Eken et al. (2012) show that large-scale anisotropy related to fabrics of the continental
102 mantle lithosphere (typically characterized by dipping symmetry axes) contaminated to-
103 mographic images in some parts of their models beneath the Fennoscandian shield and
104 concluded that this effect should not be ignored. Both O’Driscoll et al. (2011) and Eken
105 et al. (2012) reported that magnitude and anisotropic orientation could influence P-wave
106 traveltimes residuals and noted that tomography methods need to be improved, especially for
107 subduction regimes. These studies also emphasize the importance of azimuthal coverage of
108 earthquake distribution. Calculating azimuthal terms using observed SKS splitting param-
109 eters may provide a quick method as a first-order approximation. However, this approach
110 could have disadvantages, primarily because SKS phases arrive subvertically and are po-
111 larized in nearly horizontal directions, which makes them sensitive to horizontal anisotropy
112 only (O’Driscoll et al., 2011). Directly inverting for anisotropy and isotropic velocity (e.g.,
113 Eberhart-Phillips & Reyners, 2009; Ma et al., 2019; You & Zhao, 2012; Wang & Zhao, 2013;
114 Wei et al., 2019) would be a solution to overcome some of these limitations. However, data
115 availability issues mainly related to the lack of dense permanent station networks and poor
116 azimuthal coverage make the inversion even more underdetermined, and a loss in resolution

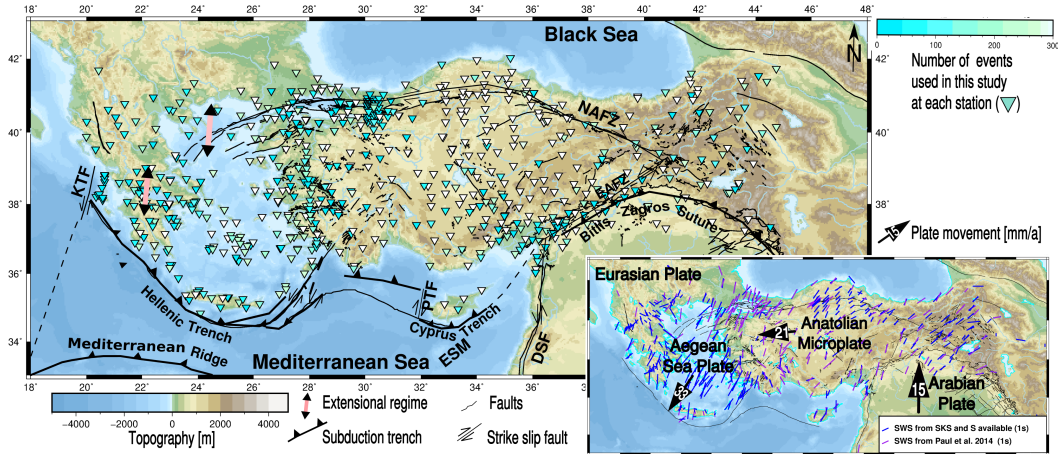


Figure 1. Topographic map of the Eastern Mediterranean and a sketch of the main active tectonic features after Taymaz et al. (2007) and Jolivet et al. (2013) and references therein. Black-pink arrows represent extensional regimes (about 15 mm/yr in the northern Aegean and Gulf of Corinth). The triangles represent stations and their respective number of waveforms used in this tomography study. Inset in the lower right shows averaged GPS vectors (black arrows in mm/yr) of the plates with respect to a stable Eurasian plate after Reilinger et al. (2006) and Le Pichon and Kreemer (2010). Anisotropy parameters from direct S-wave and SKS-wave studies in the Eastern Mediterranean were retrieved from the splitting database of Wüstefeld and Bokelmann (2007) and Paul et al. (2014). *Abbreviations:* DSF: Dead Sea Fault, EAFZ: East Anatolian Fault Zone, ESM: Eratosthenes Seamount, KTF: Kefalonia Transform Fault, NAFZ: North Anatolian Fault Zone, PTF: Paphos Transform Fault.

117 is usually the consequence when solving for additional unknowns. More recently, Bezada
 118 et al. (2016) tested the effect of anisotropy on a synthetic inversion experiment. A strain-
 119 induced LPO of upper mantle aggregates in a 3D subduction model was established prior
 120 to the tomographic inversion. They observed that artificial velocity anomalies produced by
 121 anisotropy could be up to hundreds of kilometers wide and that including estimates of the
 122 anisotropy field as a priori constraints could be useful in reducing these artifacts. Estimates
 123 of the anisotropy field could come, for instance, from numerical models that simulate the
 124 geodynamic evolution of the region and consequent mantle flow and LPO formation.

125 In this study, we invert a large number of teleseismic P-wave traveltime residuals from
 126 several permanent and temporary seismic networks that have operated in the Aegean and
 127 Anatolia. The larger and more comprehensive data set gives our model improved resolution

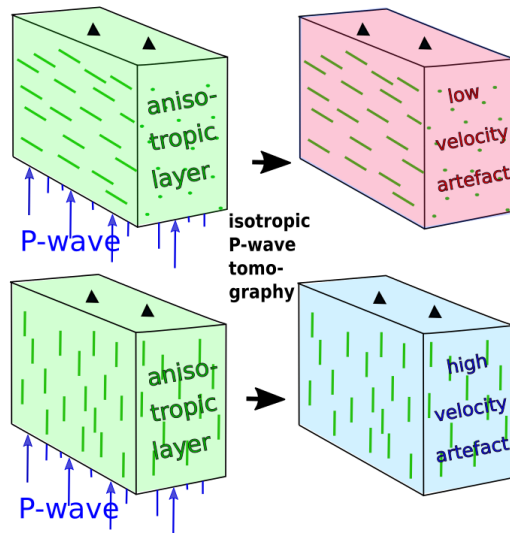


Figure 2. Sketch of an anisotropic body with horizontal (top) and vertical (bottom) FPDs on the left side. The results of a hypothetical isotropic tomography inversion show apparent low-velocity perturbations for horizontally directed FPDs (top) and high-velocity perturbations for vertically directed FPDs (bottom), on the right side respectively (if we assume vertically propagating P-waves).

128 compared to other available tomographic models (e.g., Biryol et al., 2011; Fichtner, Saygin,
 129 et al., 2013; Fichtner, Trampert, et al., 2013; Piromallo & Morelli, 2003; Portner et al.,
 130 2018), which results in novel insights into the tectonic features, of Greece and the Aegean,
 131 improving the knowledge of the velocity structures present in the upper mantle of the
 132 Eastern Mediterranean and Anatolia. In addition to the new isotropic model, to better
 133 characterize the 3D P-wave velocity anomalies, we apply a correction to our observed P-
 134 traveltime residuals using anisotropy parameters inferred from numerical models as well
 135 as SWS measurements. Discrepancies between the corrected and uncorrected tomographic
 136 models reveal the role of seismic anisotropy in changing the velocity perturbations in the
 137 upper mantle beneath this active tectonic region.

138 1.1 Tectonic Setting of the Region

139 The Eastern Mediterranean has been affected by ancient and current subduction systems
 140 since the Cretaceous (Görür, 1988), impacting the crust and generating destructive earth-
 141 quakes in the region (Taymaz et al., 2004). This study investigates the more recent subduc-

142 tion process starting in the Oligocene (Jolivet, 2001), from about 30 Ma (million years ago)
143 until the present. Currently, the Nubian and Arabian plates are actively moving toward the
144 Eurasian plate (Reilinger et al., 2006), while the Anatolian plateau is moving to the west
145 and the Aegean is characterized by an extensional regime due to subduction rollback (e.g.,
146 Le Pichon & Kreemer, 2010). Continental lithosphere is subducting at the northwestern
147 end of the Hellenic subduction system (Evangelidis, 2017; Pearce et al., 2012), while south-
148 east of the Kefalonia Transform Fault (KTF) the Ionian oceanic lithosphere is subducting
149 in a half-arc. The subduction rates at the northern Hellenic trench (continental part) are
150 much slower than at the southern trench (oceanic part) (e.g., McClusky et al., 2000), which
151 offsets the southern trench by 70-85 km at the KTF (Pearce et al., 2012). In contrast, below
152 Cyprus, the subducting slab is no longer active and is considered to be in transition to
153 continental collision similar to eastern Anatolia (e.g., Feld et al., 2017), where collision is
154 forming mountain belts in southeastern Anatolia and the Caucasus (Tan & Taymaz, 2006).
155 The Hellenic and Cyprus subduction systems have experienced tearing in several locations.
156 A geological and tectonic reconstruction study by Jolivet et al. (2013) dated the tearing
157 in southwestern Turkey to ~ 15 Ma, with subsequent slab break-off in eastern Anatolia
158 occurring around 10 Ma and the most recent tear in the Gulf of Corinth starting around
159 5 Ma.

160 Body and surface wave tomography studies (Biryol et al., 2011; Çubuk-Sabuncu et al., 2017;
161 Fichtner, Saygin, et al., 2013; Fichtner, Trampert, et al., 2013; Govers & Fichtner, 2016;
162 Portner et al., 2018; Salaün et al., 2012; Taymaz, 1996; Wei et al., 2019) indicate low-velocity
163 anomalies and separation of the Aegean and Cyprian slab in southwestern Turkey, at depths
164 between 50 and at least 300 km. They interpret this as a north-south fragmentation of the
165 Hellenic slab, which started in the Eocene-Miocene as a result of the different retreat rates
166 of the trenches. The rollback in the Aegean and the steepening of the Cyprus slab started
167 subsequently. Even thermal anomalies in western Anatolia, extending from the upper man-
168 tle into the crust, might be generated by the rollback and slab tearing (Roche et al., 2019).
169 Biryol et al. (2011) and Portner et al. (2018) found evidence for a smaller tear in the Cyprian
170 trench, defining an eastern and a western Cyprian slab and linked the tearing to volcanism
171 in the Central Anatolian Volcanic Province. Biryol et al. (2011) found a vertical tear reach-
172 ing ~ 200 km depth, while Portner et al. (2018) interpreted a horizontal tear propagating
173 from east to west in the Cyprian slab. To the south of Cyprus, the Eratosthenes Seamount
174 collided with the island and at present appears to block the subduction process (Schattner,

175 2010, and references therein). Gürer et al. (2018) dates another extensional and rollback
 176 phase related to subduction in central Anatolia to about 80-43 Ma, implying that some slab
 177 fragmentations may be older than previously thought. The latest strong extensional phase
 178 (past 10-15 million years) in the Aegean (Wortel & Spakman, 2000) as well as mantle flow
 179 through the tear and around the slab (Jolivet et al., 2018) could produce strong anisotropy,
 180 which may affect imaging the velocity structures of the upper mantle. Eastern Anatolia
 181 and Arabia started colliding about 30-35 Ma (Jolivet & Faccenna, 2000); after the closure of
 182 the Bitlis suture (16 Ma, Govers & Fichtner, 2016), the slab's dipping angle steepened. The
 183 slab most likely broke off at 10-15 Ma (Jolivet et al., 2013), making asthenospheric inflow
 184 possible. Domal uplift of the Eastern Anatolian Plateau (EAP) accompanied by volcanism
 185 (e.g., Keskin, 2003) began after the slab break-off.

186 The Anatolian crust is 38-55 km thick on the EAP (e.g., Karabulut et al., 2019; Vanacore et
 187 al., 2013), 37-47 km in central Anatolia, and approximately 30 km in the west, indicating a
 188 west-to-east crustal thickening (e.g., Mutlu & Karabulut, 2011; Vanacore et al., 2013). Due
 189 to the retreat and extension, the crust of the Aegean Sea is thinner (~ 25 km, Saunders et
 190 al., 1998; Tirel et al., 2004) than that of the surrounding plates.

191

192 **1.2 Anisotropy in the Region**

193 Several SWS studies have investigated lateral variations in the direction and strength of
 194 anisotropy in various tectonic provinces of the study area, for example, eastern Turkey
 195 (e.g., Paul et al., 2014; Sandvol et al., 2003), north-central Turkey (e.g., Biryol et al., 2010;
 196 Paul et al., 2014), western Turkey (Paul et al., 2014), the Aegean Sea and Greece (e.g., Con-
 197 fal et al., 2016; Evangelidis et al., 2011; Olive et al., 2014; Paul et al., 2014), and along the
 198 Cyprus trench (Yolsal-Çevikbilen, 2014). Anisotropic behavior in the lithosphere has been
 199 well constrained by the anisotropic inversion of Pn traveltimes residuals in the whole region
 200 (Mutlu & Karabulut, 2011) and through the analysis of the directional dependence of tele-
 201 seismic receiver functions collected at the central NAFZ (Licciardi et al., 2018). Paul et al.
 202 (2014) explained the pervasive pattern of the NE-SW fast-axis orientations from the north-
 203 ern Aegean Sea to eastern Anatolia as the result of instantaneous density-driven mantle flow
 204 in the asthenosphere with additional local effects, such as slab rollback in the Aegean Sea
 205 and a slab window beneath southwestern Anatolia. Later, Confal et al. (2018) were able to
 206 simulate such regional coherency in splitting measurements using a 3D petrological-thermo-

207 mechanical model, where a significant S-N asthenospheric mantle flow resulted from various
208 effects including, primarily, the Nubian-Eurasian plate convergence with slab rollback in
209 the Aegean Sea, a tear in the African slab, and detachment occurring within the Arabian
210 plate (break-off) (Figure 1). Observed splitting time delays of up to 2s suggest that this
211 primarily sub-lithospheric anisotropy might significantly alter isotropic velocity models at
212 these depths. In the Aegean back-arc region, FPDs are predominantly perpendicular to the
213 trench and TDs are large (1.5 ± 0.4 s Confal et al., 2016; Paul et al., 2014). In Anatolia,
214 FPDs are NE-SW oriented, while in southwestern Anatolia and the Peloponnese, the pat-
215 tern becomes more complex because of suspected slab tearing (Paul et al., 2014) and local
216 changes due to return flow (Olive et al., 2014), respectively.

217 Numerical 3D synthetic anisotropy calculations of the Eastern Mediterranean and Anatolia
218 by Confal et al. (2018) show an overall consistency with existing shear wave splitting mea-
219 surements in the Eastern Mediterranean region. Near the subducting slab, however, they
220 also suggest strong vertically directed mantle flow; thus, vertical anisotropy is likely to be
221 present. In section 4, we explore the effect of such an anisotropy field on the tomographic
222 imaging.

223 Recently, Wei et al. (2019) conducted an anisotropic inversion of P-wave traveltime data
224 based on global catalogs from beneath the Eastern Mediterranean and Middle East. They
225 later synthetically calculated path-integrated SKS splitting parameters based on the verti-
226 cally stratified FPDs of P-waves resolved from the inversion. A comparison between their
227 synthetic SKS splitting parameters and those observed from previous SWS studies revealed
228 similar patterns; for example, NE-SW-oriented FPDs in most of Anatolia, a circular pat-
229 tern around the tear in southwestern Anatolia, and trench-parallel FPDs in the fore-arc and
230 sub-slab regions. It is only in the central-south Aegean that the synthetically estimated
231 TDs are very small, a result that contradicts to the seismic observations reported in Paul et
232 al. (2014) and Confal et al. (2016), and the numerical models of Confal et al. (2018). Such
233 inconsistencies may stem either from the damping and smoothing parameters used in the
234 regularization of the inverse problem, or the insufficient amount of P-waves or SKS-phase
235 data recorded in those regions.

236 **2 Data**

237 In this study, we invert relative P-wave traveltime residuals to obtain a model of 3D P-
238 wave velocity perturbations in the upper mantle. Measurements were made on records from

239 686 broadband and short-period seismic stations located between 20-48°EW and 33-43°NS
 240 in a region covering the Aegean, Anatolia, Greece, and Georgia (Figure 1). The seismic
 241 stations belong to several seismographic networks with digital seismic waveform recordings
 242 extracted for the years 2005-2010 and 2013-2015. Most stations utilized in this study are
 243 operated by the Regional Earthquake-Tsunami Monitoring Center (KOERI-RETMC). We
 244 also used data recorded by several regional seismic stations operated by the Greek National
 245 Observatory of Athens (NOA-IG). Furthermore, three-component data from 72 broadband
 246 seismic stations in central Anatolia, which operated between 2013 and 2015 as part of the
 247 Continental Dynamics-Central Anatolian Tectonics project (CD-CAT, Sandvol, 2013), were
 248 also used.

249 We selected 1,135 teleseismic events with magnitudes $M_w > 5.0$ and epicentral distances
 250 between 30° and 90°. Following a visual inspection process, we consider the P-wave arrival
 251 times for 935 earthquakes for further analysis, since some of the observed data had unaccept-
 252 ably low signal-to-noise ratio. To obtain relative arrival times and uncertainty estimates, we
 253 used multi-channel cross-correlation (VanDecar & Crosson, 1990) with three center frequen-
 254 cies, 1 Hz (22.9% of data), 0.5 Hz (32.6%) and 0.3 Hz (44.6%). This enabled us to obtain
 255 up to three sets of relative delays for each event. After cross-correlating the data, 557 good
 256 events producing 107,283 frequency-dependent delays were used for the inversion (Figure S1
 257 in the supporting information). The backazimuthal distribution is somewhat uneven (with
 258 more events between 5° and 110° than between 111° and 4°) due to epicentral distance
 259 limitations, yet events of nearly all backazimuths are represented in this study (Figure S1).

260 **3 Method**

261 We use the hybrid ray-tracing method of Bezada et al. (2013) for isotropic delay calcu-
 262 lations. This method combines velocity-dependent iterative ray-tracing and approximate
 263 finite-frequency Born kernels (Bezada et al., 2013; Schmandt & Humphreys, 2010). Travel-
 264 times outside the model volume are calculated using a 1D model, whereas the times inside
 265 the box are calculated using a 3D velocity model applying the graph-theory-based method of
 266 Toomey et al. (1994). As a background model, for the initial ray paths and the calculation
 267 of sensitivity kernels, we employ the AK135 1D velocity model of Kennett et al. (1995). For
 268 the inversion, we use a study area approximately 2,000 km (E-W) by 500 km (N-S), with a 30
 269 to 50 km vertical (increasing with depth) and 42 to 56 km horizontal (increasing toward the
 270 edges of the model) node spacing, resulting in 69x39x24 (x y z) nodes (64,584 nodes in total,

271 Figure 3c). Our model extends from 750 km depth to the Earth’s surface. To overcome the
272 limited resolution and contamination of the model resulting from unimaged anomalies in the
273 lithosphere above 50 km, the surface wave velocity model of Delph et al. (2015) is used as a
274 constraint for about 80% of our study area. The S-wave velocities are converted to P-wave
275 velocities with an average V_p/V_S ratio of 1.8, adopted from a recent receiver function study
276 by Schiffer et al. (2019). The compiled data are implemented into our starting model to
277 represent the crustal structure prior to the inversion. High damping values prevent model
278 velocities in the crustal block from significantly changing in subsequent iterations (Bezada
279 et al., 2013). We prefer this approach over static corrections derived from crustal thickness
280 because it accounts for the effect of crustal velocity variations on ray tracing and includes
281 the effect of lateral variations in sedimentary basin thickness. The crustal structure in our
282 final model closely resembles the model of Delph et al. (2015) but with slightly poorer reso-
283 lution. In regions where we do not have crustal structure information, no prior constraints
284 are placed on the inversion. In the present work, we will discuss only the structures and
285 anomalies deeper than 60 km, since the focus of this study is on upper mantle structures and
286 anisotropy. In order to regularize the inversion, constraints on the model norm and model
287 roughness are imposed on the model. After the first iteration, the delays are recalculated in
288 two additional iterations, sufficient for the model to stabilize. In addition to P-wave velocity
289 model parameters, we inverted for station and event parameters.

290 Damping and smoothing parameters for the inversion were carefully selected and applied in
291 such a way that the norm and roughness of the total model (rather than the updates to the
292 model) are minimized in each iteration. We calculated the variance reduction and L2 norm
293 for damping values of 1 to 11 and smoothing values of 1 to 14 resulting in 154 different
294 models. We selected the best parameters using an L-curve for the first iteration (see Figure
295 S4 and Table 1). Additionally, we looked at the misfit with norm and mean curves of the
296 relative residuals (Figure S3). We calculated hit quality maps for each depth layer (Figure
297 S5), to evaluate the quality of the sampling of the model space. Our hit quality metric is
298 based on the number of rays in a node and takes the backazimuthal distribution into account
299 (Schmandt & Humphreys, 2010). The hit quality is good (>0.4) in nearly the whole study
300 area in depths ranging from 100 to 300 km. It is noted that underneath two offshore regions
301 in the Aegean that have small station coverage is the hit quality lower at about 0.3-0.4.
302 Depths greater than 300 km and regions towards the edges of the model lose resolution.
303 The resolution of the checkerboard test is very good in the upper 300 km (Figures S6 and

304 S7). Toward the edges of the model, and with depth, some smearing and amplitude loss
 305 of perturbations is visible (Figure S6). In the eastern part of the model, data resolution
 306 seems to be problematic, resulting in smearing and difficulties in resolving small structures
 307 (Figure S7).

308 **4 P-wave Tomography Corrected for Anisotropy**

309 To include anisotropy in our velocity perturbation calculations, we used an approach that
 310 has been described and successfully tested on a synthetic data set in Bezada et al. (2016).
 311 Delay calculations are processed similarly to fully isotropic cases (see section 3), except in-
 312 cluding prescribed *a priori* anisotropy. The assumed anisotropy field, inferred from various
 313 sources (e.g., numerical model or shear wave splitting measurements), is interpolated into
 314 the ray-tracing grid and included in the forward traveltimes calculations. As a result, each
 315 delay has a unique correction that depends on its corresponding ray-path. The 3D ray-
 316 tracing method is limited to anisotropy with a hexagonal symmetry for simplicity (Toomey
 317 et al., 1994); therefore, the elastic tensors from the numerical model are approximated to the
 318 best-fitting hexagonal symmetry tensors with D-REX (Browaeys & Chevrot, 2004; Kaminski
 319 et al., 2004). In the first iteration, the prescribed anisotropy field is included in the
 320 reference velocity model and the input delays are recalculated. In principle, this removes
 321 the effect of the assumed anisotropy from the delays. For every following iteration, delays
 322 are recalculated by considering the updated isotropic structure from the previous iteration
 323 and the anisotropy field. We define *a priori* anisotropy fields for two different cases (Figure
 324 3):

- 325
- 326 1. Numerical model: Anisotropy parameters based on the numerical model of the region
 327 by Confal et al. (2018) are introduced to the starting model prior to the tomographic
 328 inversion. The strength of seismic anisotropy and its direction are calculated (D-
 329 Rex Faccenda & Capitanio, 2013; Kaminski et al., 2004) using the mantle flow and
 330 temperature yielded from the numerical reconstruction of the tectonic evolution of
 331 the study area over the past 22 million years. When including the 3D anisotropy of
 332 the numerical model in the inversion, some geometric adjustments were made to fit
 333 the real geometry of the region. The anisotropy taken directly from the numerical
 334 model (Confal et al., 2018) resulted in calculated SKS splits that were larger than
 335 the observed splits by a factor of ~ 2 , most notably in the Aegean region; thus, the

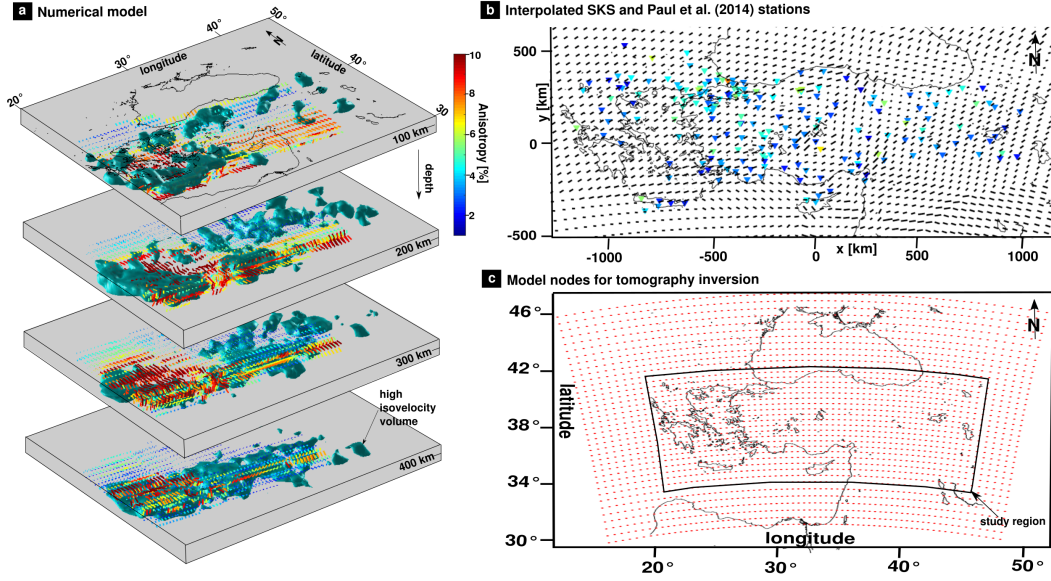


Figure 3. a) 3D anisotropy (colored bars) of the adjusted numerical model (Confal et al., 2018) and isotropic high-velocity structures (cyan, see also Figure 8) on four 100 km thick depth slices. For the inversion, the anisotropy strength of the numerical model is halved. b) Black bars are interpolated anisotropy directions and the triangles are source stations for the interpolation of SKS measurements of Paul et al. (2014) with their respective strength of anisotropy (same color scheme as a). c) Red dots are the model nodes of the isotropic and anisotropy-corrected tomography inversions.

336 anisotropy fractions were halved. The modeled half-arc region of the Aegean was
 337 flipped to complete the actual full arc of the Hellenic trench. To fit the geometry of
 338 the slab, the model was sheared with depth and rotated toward the east by 5° . The
 339 EW direction was scaled to 65% of its original size and the NS to 35%, respectively
 340 (Figure 3a).

341 2. Observational constraints (SKS-wave measurements): We assume that the shear wave
 342 splitting is the result of a single layer of anisotropy with a laterally variable but
 343 vertically homogeneous fast polarization direction and anisotropy strength (Figure
 344 3b). At each point, the fast direction of propagation is the same as the average FPD
 345 observed directly above, and the percentage of anisotropy is such that integrated over
 346 the thickness of the layer (placed at 90 to 350 km depth), it results in the observed
 347 TDs. The SWS parameters of Paul et al. (2014) were used since they cover the entire
 348 study area.

Table 1. The minimum and maximum velocity perturbation, total variance reduction (TVR), L2 Norm and Root Mean Square (RMS) values for selected models (isotropic and models corrected for anisotropy from a numerical model and SKS measurements) after the third iteration.

Model	Description	Min. [%]	Max. [%]	TVR [%]	L2 Norm	RMS [s]
Run62	Isotropic	-14.22	10.14	74.32	3.35	0.3831
Run198	Numerical Model	-13.66	10.51	75.90	3.45	0.3845
Run201	SKS	-11.95	11.27	74.87	3.40	0.3837

5 Results

5.1 P-wave Tomography With Isotropic Starting Model

Our preferred model uses damping (4) and smoothing (8) values determined through an L-curve analysis and achieves a variance reduction of 74.68% and L2 norm of 3.33 in the first iteration of the isotropic model; the same damping and smoothing values are used for the inversions corrected for anisotropy.

In western Greece and the southern Aegean (between $\sim 20^\circ$ and 28° longitude), a high-velocity semicircular-shaped structure that follows the Hellenic subduction trench is visible (Marker 1, Figures 4a, 5a, 7a1, and S9 at 60-690 km). In the west, north of the KTF, inside the high-velocity structure, an embedded low-velocity structure appears to exist parallel to the trench (NW-SE directed) present above 160-km depth (Marker 2, Figure 4a). In the southern Aegean, the high-velocity structure is approximately 200-300 km thick. Below 90 km depth, beneath Crete, it dips north with a 60° angle until it flattens ($10\text{-}20^\circ$ dip angle) after the ~ 410 km discontinuity (Marker 1, Figures 7a1, and S10). In the east, the high-velocity structure is not connected to the Cyprian slab at shallower depths (Marker 3, Figure 4a). First-order low-velocity structures (about 50-100 km wide and 100-200 km long) at 60- to 450 km depths occur in the model (Marker 3/4, Figures 4a, 5a, 7b1). They appear to reside inside or in close proximity to a large deep gap in the high-velocity structure. The high-velocity anomaly underneath Cyprus and western Anatolia dips more steeply and appears to be fragmented. A western Cyprian slab (WCS) fragment is thin at shallow depths and becomes a thick bulge at 190 to 230 km depth (Marker 5, Figure 4a). An eastern Cyprian slab (ECS, Marker 6, Figure 4a) starts south of Cyprus but connects with the WCS at about 250-km depth (Marker 7 in Figure 4a). Toward the east, beneath the Bitlis Zagros

372 suture zone, some high-velocity fragments 100-200 km wide at 200 to 400 km depth can be
 373 seen (Marker 8, Figures 5a and 7d1). Beneath the central Aegean, the uppermost mantle
 374 is mostly free of intense anomalies. There is a high-velocity anomaly at depth shallower
 375 than ~ 200 km beneath the region of Istanbul and northern Anatolia (Marker 9, Figures 4a
 376 and 7c1). Farther south, in central and eastern Anatolia, three large and deep low-velocity
 377 structures can be found down to a depth of 300 km, separated in the deeper parts but
 378 connected in the upper 50 km of the model (Marker 10, Figures 4a and 7c1/d1).

380 **5.2 P-Wave Tomography With an Anisotropic Starting Model**

381 When performing the inversion with *a priori* constraints on anisotropy, most first-order
 382 velocity perturbations (i.e., subducting and fragmented slab, tear and break-off in the slab,
 383 and significant low-velocity zones in eastern Anatolia) are similar to those resolved after
 384 isotropic inversions. Nevertheless, some important features have significant differences in
 385 the shape and magnitude of the velocity variations (Figures 4-6, marked with a green circle
 386 and an uppercase letter).

387 A comparison of synthetic tests (see Figure S8) suggests that even minor features can be
 388 resolved from all of our inversions and that the effect of anisotropy on the delay times
 389 surpasses the impact of presumable noise, especially with a standard deviation of 0.1 s,
 390 which can be regarded as a reasonable range for data error (e.g., Timkó et al., 2019). When
 391 introducing noise with a standard deviation of 0.2 s, the range of velocity perturbation
 392 differences, compared to the purely isotropic case, becomes similar to the case obtained
 393 when anisotropy was added. Our synthetic tests imply that anisotropy-induced artifacts
 394 are most prominent and distinct with respect to the random noise effect mainly around the
 395 subduction zone, where mantle flow is likely to be more vigorous.

396 ***5.2.1 Main Differences of the Tomography Including Anisotropy From a Nu-*** 397 ***merical Model***

398 When comparing the isotropic models, derived with and without using *a priori* constraints
 399 on anisotropy from the numerical model of Confal et al. (2018) (Figure 6), the maximum
 400 discrepancies for velocity perturbations are -5.8% (the isotropic model is slower) and 5.2%
 401 (the isotropic model is faster). More than 52% of all nodes are faster in the isotropic
 402 inversion, while nearly 48% are slower. The average of the differences is the same with

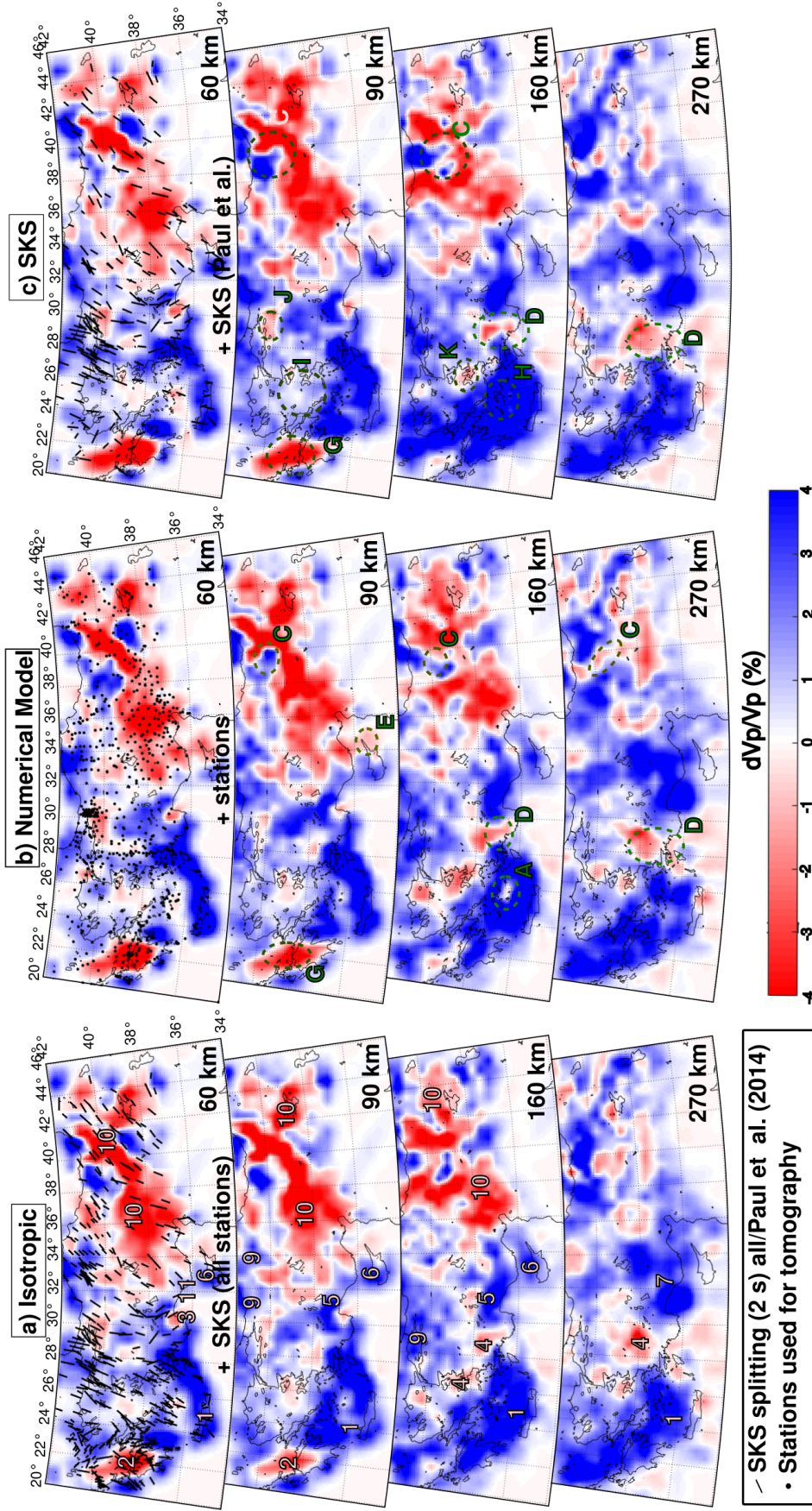


Figure 4. Part one: Horizontal slices of P-wave velocity perturbations in the upper mantle a) with an isotropic starting model, b) with an anisotropic starting model based on the numerical computation of Confal et al. (2018) and c) with an anisotropic starting model based on the SKS splitting observations by Paul et al. (2014). On the 60 km depth slice a) all available shear wave splitting measurements of the region, b) stations used for the inversion and c) SKS splitting observations by Paul et al. (2014) are plotted. For each model a smoothing factor of 8 and damping of 4 was used, above 50 km the velocity model of Delph et al. (2015) was used for crustal corrections. Dark green letter markers and dashed circles are referenced in the text.

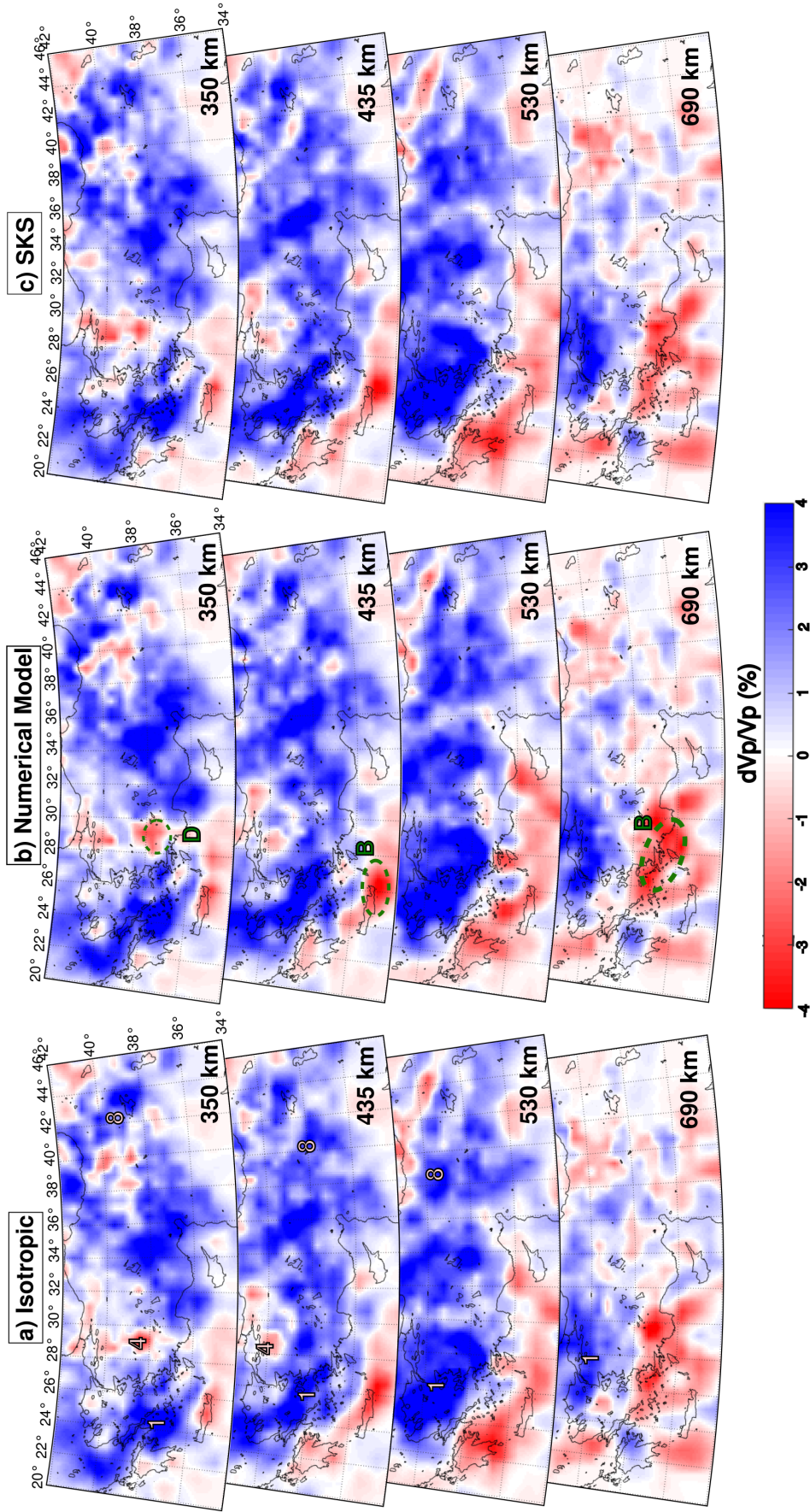


Figure 5. Part two: Horizontal slices of P-wave velocity perturbations in the upper mantle with a) an isotropic starting model, b) an anisotropic starting model based on the numerical computation in Confal et al. (2018) and c) an anisotropic starting model based on SKS splitting observations by Paul et al. (2014).

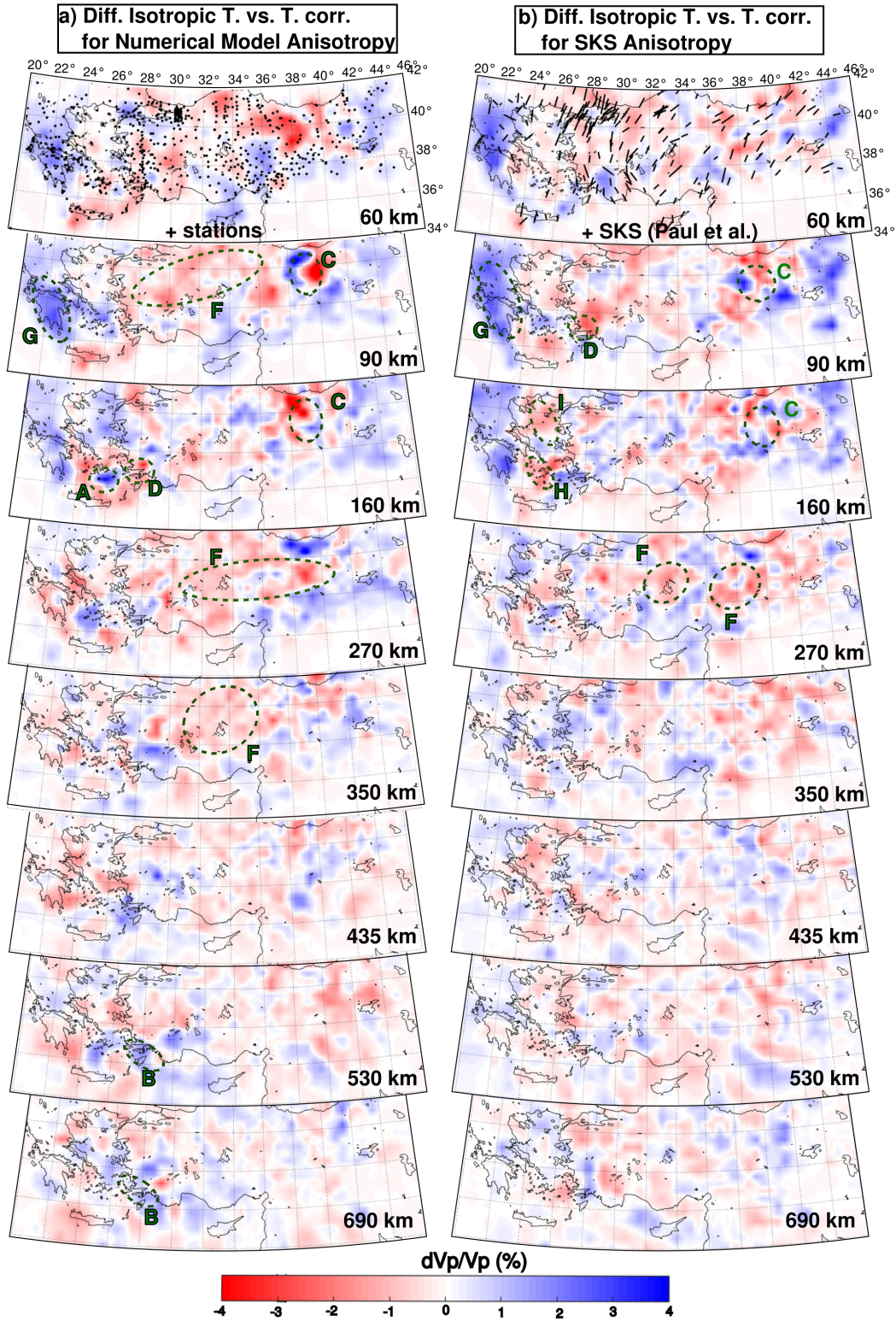


Figure 6. Horizontal slices of discrepancies between uncorrected and anisotropy-corrected P-wave velocity perturbations. Corrections were made with (a) an anisotropic starting model based on the numerical computation in Confal et al. (2018) and (b) an anisotropic starting model based on SKS splitting observations by Paul et al. (2014). *Abbreviations:* Diff.: Difference, T.: Tomography, corr.: corrected.

403 0.16% for high-velocity and low-velocity. Only 3.23% of the model is more than 1% different
 404 (1.57% isotropic faster, 1.66% isotropic slower). Most first-order structures are in the same
 405 locations but may differ in their geometry.

406 In anisotropically corrected images, the low-velocity structure below western Greece seems
 407 to be stronger and larger with respect to the one resolved in the isotropic model. To a depth
 408 of 230 km, the high-velocity anomaly in the southern Aegean becomes thinner or splits in two
 409 parts (Marker A, Figure 4b). The slab low-velocity anomaly is slightly stronger when we
 410 introduce numerically modeled anisotropy (Marker B, Figures 5b and 7a2). In northeastern
 411 Turkey, low and high-velocity perturbations exhibit prominent variations ($\pm 2-3\%$) without
 412 a clear pattern (Marker C, Figures 4b, 6a, and 7d2). The low-velocity anomalies between
 413 the Hellenic and Cyprus high-velocity perturbations differ in their shape (Marker D, Figure
 414 4b, 5b, and 6a). South of Cyprus, there is an additional small low-velocity zone to the
 415 east of the high-velocity zone (Marker E, Figure 4b), which is dismissively small in the
 416 isotropic model. Low-velocity anomalies underneath the Central and Eastern Anatolian
 417 Plateau (CAP and EAP) appear to be 1-3% more intense between 230 and 270 km depth
 418 in the inversion that includes anisotropy from the numerical model (Marker F, Figure 6a).

419 *5.2.2 Main Differences of the Tomography Including Anisotropy From SKS* 420 *Measurements*

421 In addition to using a starting model with numerically derived estimates of anisotropy,
 422 we also invert our observed traveltime residuals with a second anisotropic starting model,
 423 which is based on the available SKS splitting measurements for the entire region reported
 424 in Paul et al. (2014). A comparison between uncorrected isotropic tomography images and
 425 those corrected for anisotropy using SKS splitting measurements (Figure 6), displays values
 426 ranging from a minimum of -5.44% (isotropic slower) to a maximum of 4.54% (isotropic
 427 faster). The fraction of slower nodes in the isotropic version is 47% (difference average=-
 428 0.18%) while fast nodes represent 53% (difference average=0.17%). Of the nodes 3.59% are
 429 more than 1% different (1.83% isotropic faster, 1.76% isotropic slower). The low-velocity
 430 structure underneath western Greece appears to be even stronger and larger than in the
 431 tomography that includes anisotropy from the numerical model (Marker G, Figure 4c and
 432 6b). Starting at a depth of 125 km the high-velocity anomaly in the southern Aegean ap-
 433 pears to be thicker, and there is no gap visible in the slab as seen in the model corrected
 434 for numerical anisotropy (Marker H, Figures 4c and 6b). In the northern Aegean and the

435 rollback area, the isotropic tomography is about 1-2% slower at depths down to 230 km
436 (Marker I, Figures 4c, 6b, and 7a3). A low-velocity anomaly present south of Istanbul ap-
437 pears to be stronger at 90 km depth (Marker J, Figure 4c), and in the upper 200 km, another
438 low-velocity anomaly in western Anatolia is weaker than in the model corrected for numer-
439 ically calculated anisotropy (Marker K, Figure 4c). High and low-velocity perturbations
440 in northeastern Anatolia differ by $\pm 2-3\%$ from the isotropic model as in the model with
441 numerical anisotropy, but in different locations (Marker C, Figures 4c, 7d3, and 6b).

442 **6 Discussion**

443 In this study, we showed that anisotropy can affect velocity perturbations in some areas, with
444 local differences of up to 2% compared to an isotropic tomography approach. While most
445 discrepancies between the models seem small if our primary target is to detect and prove the
446 existence of a slab, others might be relevant for the interpretations of mantle heterogeneities.
447 In cases where the exact geometry or presence of relatively small-scale anomalies, like tears
448 and fragments of the slab, are sought and if estimating the temperature of anomalies is
449 the goal, then small variations might be meaningful. In the following subsections, we will
450 discuss the stable and prominent features of this P-wave tomography that are visible in all
451 of the models and examine the differences between isotropic models and models corrected
452 for anisotropy.

453 **6.1 Hellenic Subduction System and Aegean**

454 In isotropic tomography models (Biryol et al., 2011; Portner et al., 2018, and this study),
455 the dipping high-velocity anomaly, which is commonly explained by a subducting crust
456 and lithosphere, appears to be thicker than those expected by other methods (8- to 10-km
457 oceanic crust, 70-to 80-km Nubian lithosphere, Kind et al., 2015; Pearce et al., 2012). The
458 smearing of high-velocity anomalies is highly possible and most likely stems from an insuf-
459 ficient number of crossing rays in a given cell, which could make the slab appear thicker
460 (Bezada et al., 2016). On the other hand, the checkerboard test (Figure S6) shows no smear-
461 ing for the upper 300 km. In our tomographic images obtained after anisotropy-correction
462 using mantle flow modelling results, the slab appears to be more defined and some high-
463 velocity perturbations north of the slab in the southern Aegean are reduced (Marker A,
464 Figure 4, 90 to 160 km). Based on numerical models (e.g., Confal et al., 2018; Faccenda,
465 2014) we know that vertically/subvertically aligned anisotropy exists below and inside the

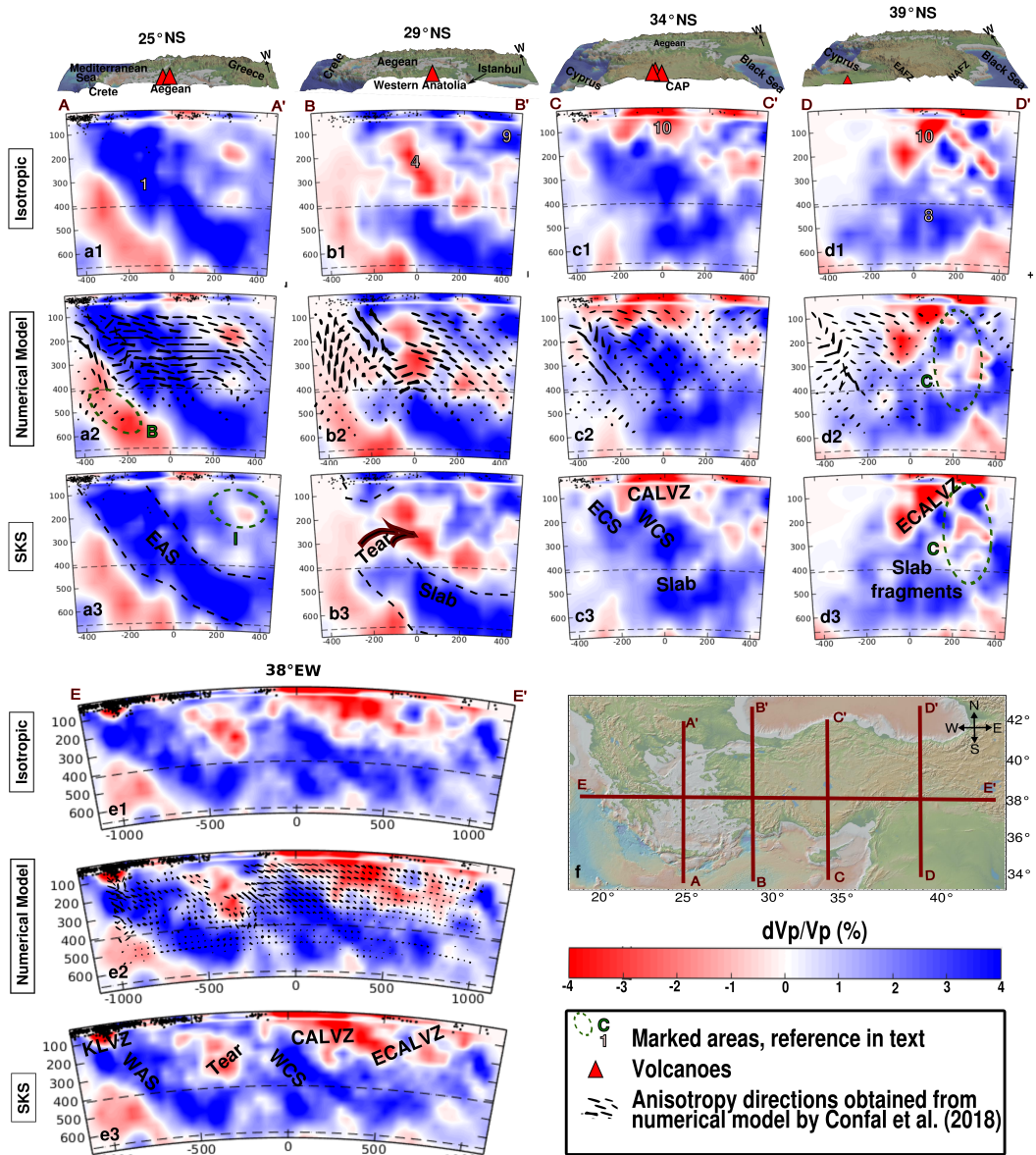


Figure 7. Cross-sections of three different P-wave tomography models (1-3) with some marked areas (reference in the main text). Four north-south cross-sections (a1, b1, c1, d1) of the isotropic model are shown. Beneath are the cross-sections of the tomography model corrected for the numerical model (a2, b2, c2, d2) and the respective anisotropy vectors on a 100 km wide slice. The tomography, including SKS measurements (a3, b3, c3, d3), is situated beneath with interpreted first order features. An east-west profile of the previously mentioned three models with the same features is presented (e1-e3). The corresponding cross-sections are marked on a map in f). The top 3D topography plots are made using GeoMapApp. *Abbreviations:* CAP: Central Anatolian Province, EAFZ: East Anatolian Fault Zone, EAS: East Aegean Slab, ECS: Eastern Cyprian Slab, CALVZ: Central Anatolian Low-Velocity Zone, ECALVZ: East-Central Anatolian Low-Velocity Zone, KLVZ: Kefalonia Low-Velocity Zone, NAFZ: North Anatolian Fault Zone, WAS: West Aegean Slab, WCS: Western Cyprian Slab.

466 slab, and in the fore-arc and back-arc regions above the mantle wedge. However, considering
467 the effect of anisotropy, the geometry does not change drastically. Therefore, smearing and
468 difficulties to resolve the half-arc geometry of the slab in tomography models might still be
469 a problem, as discussed in Portner et al. (2018).

470 Bezada et al. (2016) described a trench-parallel low-velocity artifact below a hypothetical
471 slab structure and a decrease in the strength of the anomaly when anisotropy is included.
472 Piromallo and Morelli (2003) ascribed the observed low-velocity anomaly present below the
473 Aegean slab to a possible mantle upwelling. We observe this low-velocity anomaly in all
474 three models (similar to Biryol et al., 2011; Portner et al., 2018) as it appears even more
475 intense in the models corrected for anisotropy (e.g., Marker B, Figures 5b and 7a2). The lit-
476 erature implies the low-velocity anomaly may be due to hot uprising material or sub-parallel
477 mantle flow. In a recent tomography study of Wei et al. (2019), this low-velocity anomaly is
478 less intense and only seen close to the Cyprian trench. Very strong, trench-parallel FPDs in
479 their study, identified as mantle flow, and a larger study area could explain the abundance
480 of this low-velocity anomaly compared to observations in our study. VanderBeek and Fac-
481 cenda (2020) found low-velocity artifacts, especially beneath the slab, to be very persistent,
482 when performing realistic anisotropic inversions. Sub-slab anisotropy might be difficult to
483 correct for, but a better representation and inclusion of stations from the south of Crete
484 could reduce low-velocity artifacts.

485 In the north-western segment of the Hellenic trench, high-velocity anomalies are less strong
486 or totally absent at shallow depth (<160 km), contrary to a P-wave tomography model
487 that was originally developed by Amaru (2007) and most recently interpreted in Handy et
488 al. (2019). All of our models indicate the presence of a strong, shallow (depths < 160 km,
489 Marker 2, Figures, 4, 8, and S10), low-velocity anomaly parallel to the trench (Kefalonian
490 Low-Velocity Zone, KLVZ) in south-western Greece similar to the findings of Piromallo and
491 Morelli (2003), Hansen et al. (2019), Wei et al. (2019), and Özbakır et al. (2020). Hansen
492 et al. (2019) interpret the low-velocity structure at 150 to 250 km depth as a trench-parallel
493 tear propagating through disrupted but not completely detached slab lithosphere. The shal-
494 low slab segment in western Greece ends in the S-wave tomography of Pearce et al. (2012)
495 at about 100-km depth, and there is an absence of deep earthquakes (Figure S11, beneath
496 100 km) in the same region as well. Wei et al. (2019) located a possible detachment between
497 60 and 100 km. Recently, Özbakır et al. (2020) interpreted the tear as a semi-horizontal
498 proto-STEP (Subduction-Transform-Edge-Propagator) tear until a depth of about 130 km

499 in their full-waveform tomography. Their findings fit very well with our results, in which we
 500 see a low-velocity structure parallel to the trench in 60 to 150 km depth. The slab fragmen-
 501 tation seems to have proceeded from the NW to SE ending at the KTF, which marks the
 502 border of the continental and oceanic subduction regimes. Contrary to the interpretations
 503 of some studies (Evangelidis, 2017; Guillaume et al., 2013; Jolivet et al., 2013), this study
 504 shows that this disruption in the western Hellenic slab does not seem to be a vertical tear
 505 but rather a horizontal (Hansen et al., 2019) or semi-horizontal (Özbakır et al., 2020) shal-
 506 low break-off. Nevertheless, we support the theory that this recent break assisted the fast
 507 retreat of the Hellenic slab in the southern Aegean.

508 The subduction angle of the Hellenic slab in the southern Aegean is approximately at 60° ,
 509 similar to Portner et al. (2018) but steeper than what Biryol et al. (2011) suggested. Even
 510 though the resolution decreases with depth, it is sufficient to show that the dip angle de-
 511 creases to about $10\text{-}20^\circ$, it appears to become stagnant (Figures 5 and 8c), but others, for
 512 example, Portner et al. (2018), have shown the Hellenic slab to extend further into the
 513 mantle.

514 **6.2 Slab Tear of South-Western Anatolia and the Cyprus Subduction System**

515 The tear beneath western Turkey is very well developed from shallow depths to nearly
 516 600 km, similar to earlier studies (Biryol et al., 2011; Portner et al., 2018). Low-velocities
 517 within the tear zone to the north and south (Marker 4, Figures 4 and 7) can be interpreted
 518 as volatile rich mantle inflow from below the slab. The volume and the exact locations of
 519 the anomalies differ in our three models depending on the anisotropy model used for the
 520 corrections. Paul et al. (2014) attributed the NW-SE oriented FPDs inferred from SKS
 521 splitting measurements in south-western Anatolia to the effect of toroidal mantle flow. In
 522 fact, numerical models in Confal et al. (2018) have since shown mantle flow with an anti-
 523 clockwise toroidal pattern moving through a tear towards the west, a result of the retreat
 524 of the Hellenic trench. Toward the east, the tear is connected to the smaller Cyprian tear
 525 (Marker 11, Figures 4a and 8b/c). As reported in Biryol et al. (2011) and Wei et al. (2019),
 526 the Cyprian slab is resolved as being fragmented in this study, but not by a purely horizontal
 527 tear as recently suggested by Portner et al. (2018). In our model, the shallow Cyprian tear
 528 is probably connected to the larger tear beneath western Turkey between 60 and 100 km
 529 depth that separates the western and eastern Cyprian slab (WCS and ECS) down to a depth
 530 of about 250 km. Our results correlate well with the locations of detected seismicity in the

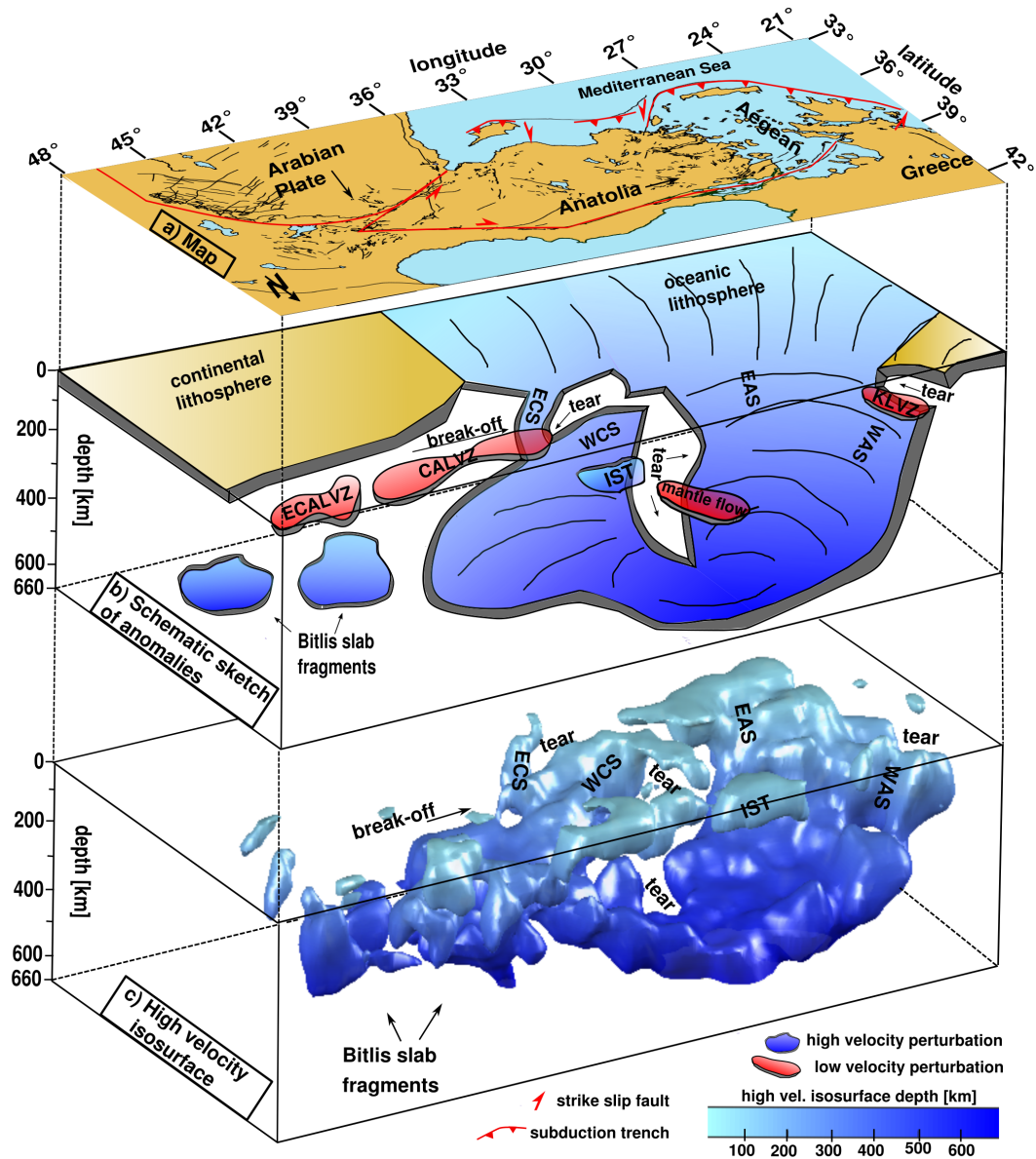


Figure 8. a) Top layer is a sketch map of the Eastern Mediterranean, with sea and lake regions in light blue and land areas in yellow. Main faults are marked with red lines and subduction zones are marked with red triangles. b) 3D sketch with important features that are interpreted and discussed in this study. c) Smoothed high-velocity perturbations above 2.5% of the tomography image corrected for anisotropy from the numerical model of Confal et al. (2018). The colorbar represents the depth of the high-velocity structure. Interpreted locations of slab detachments and important high-velocity structures are added. *Abbreviations:* CALVZ: Central Anatolian Low-Velocity Zone, EAS: East Aegean Slab, ECALVZ: East-Central Anatolian Low-Velocity Zone, ECS: Eastern Cyprian Slab, IST: Istanbul Zone, KLVZ: Kefalonia Low-Velocity Zone, WAS: West Aegean Slab, WCS: Western Cyprian Slab.

531 region (Figure S11) that indicate no shallow events south of the Antalya basin but the pres-
532 ence of deep ones in the WCS. A lack of earthquakes correlates with the Paphos Transform
533 Fault (PTF). The ECS is thin (similar to Piromallo & Morelli, 2003, at 150 km depth) but
534 continuous, starting south of Cyprus and connecting with the WCS at a depth of about
535 250 km. An absence of deeper earthquakes suggests that the ECS is not moving except for
536 in the upper 70 km (Figure S11). It is likely that the subduction process was disrupted
537 about 3 Ma, when the Eratosthenes Seamount collided with the Cyprus slab (Schattner,
538 2010, and references therein). Portner et al. (2018) suggested buoyancy-driven tearing due
539 to the denser oceanic plate of the WCS and the continental ESC. East of Cyprus, strike slip
540 faults mark the end of the subduction due to continent-continent collision and a transition
541 to slab break-off (Schattner, 2010, and references therein).

542 Westward-directed mantle flow through the various tears resolved in this study, could facil-
543 itate the westward escape movement (Schildgen et al., 2014) of the Anatolian microplate.

544 **6.3 North, Central, and Eastern Anatolia**

545 Beneath the Istanbul and Pontides block, north of the NAFZ, a prominent shallow (depth
546 < 150 km) high-velocity structure (Marker 9/IST, Figures 4a, 7c1, and 8), similar to those
547 seen in the models of Biryol et al. (2011) and Portner et al. (2018), is clearly visible and
548 could be related to Neotethyan sutures (e.g., Biryol et al., 2011; Okay & Tüysüz, 1999;
549 Salaün et al., 2012). Similar to Portner et al. (2018), we see a relatively sharp border from
550 high averaged velocity perturbations in the west to low averaged velocity perturbations in
551 the east in central Anatolia (Figure S2). Shallow low-velocity perturbations beneath the
552 CAP (Central Anatolian Low-Velocity Zone, CALVZ) correspond well with similar findings
553 of Biryol et al. (2011) and Portner et al. (2018), as well as with the results of the full wave-
554 form tomography of Fichtner, Saygin, et al. (2013). Weak lithosphere (e.g., Delph et al.,
555 2017) and tearing in the Cyprian slab (e.g., Portner et al., 2018, and this study) possibly
556 facilitated the upwelling of hot asthenospheric material and active volcanism. The recent
557 uplift in this region could be a consequence of the rebound of the subducting lithosphere
558 after the shallow break-off (Delph et al., 2017; Schildgen et al., 2014), equally asthenospheric
559 inflow beneath central Anatolia could also be responsible for the uplift (e.g., Cosentino et al.,
560 2012; Govers & Fichtner, 2016). Velocity anomalies in our study suggest that the Cyprian
561 slab has not totally broken-off beneath central Anatolia, which is in contrast to the latest
562 tomography findings of Portner et al. (2018). More precisely, our models show that it is

563 connected with the gently dipping deeper parts of the Hellenic slab (Figure 8b). There-
564 fore, we suggest recent uplift is not responsible for the rebound but is mostly the result
565 of asthenospheric melt inflowing through the tear between the Cyprean slabs. The trench
566 retreat slowed down (Schildgen et al., 2014); therefore, extension is absent in this region
567 and thinning of the crust has not occurred.

568 The slab detachment beneath the Bitlis Zagros suture zone seems to be at an advanced
569 stage, with no large continuous slab and close to no earthquake activity below 20 km (Fig-
570 ure S11). In central Anatolia, the relic slab lies at about 400-km depth and is connected to
571 the Hellenic slab. Biryol et al. (2011) suggested a stagnated slab at the mantle transition
572 zone, while Portner et al. (2018) did not find any evidence of a slab present beneath central
573 and eastern Anatolia. In our tomography, it appears that the Cyprian slab (which reaches
574 400 to 500 km depth) never sunk as deep as the Hellenic slab (until 500 to 660 km depth),
575 although they are connected. The slab may be stuck, and this could be preventing it from
576 sinking deeper due to the collision with the Eratosthenes Seamount (e.g., Biryol et al., 2011;
577 Schattner, 2010). Although resolution decreases with depth and towards the east, Bitlis
578 slab fragments beneath eastern Anatolia (roughly cubic high-velocity anomalies with side
579 lengths of 50-100 km) can be distinguished (Figure 8c).

580 Given the insufficient data coverage in eastern Anatolia, our model resolution of this region
581 might be relatively poor and may generate artificial anomalies. While the normalized hit
582 quality values of 0.4-0.5 indicate reasonably good data resolution (Figure S5), the checker-
583 board test shows smearing in this region, implying that the results may not be sufficiently
584 robust for interpretation.

586 **6.4 Uncorrected Isotropic Model Versus Models Corrected for Anisotropy**

587 Previous studies have shown that whether anisotropy is neglected in tomographic inversions
588 or some effort is made to account for its effect, the main features recovered are generally
589 stable, with second-order differences between the models often present (e.g., Bezada et al.,
590 2016; Eken et al., 2012; Lloyd & van der Lee, 2008; O'Driscoll et al., 2011; Sobolev et al.,
591 1999). Even when anisotropy is explicitly solved for in the traveltimes inversion, a similar
592 scale of differences is found between isotropic and anisotropic models (e.g., Ishise & Oda,
593 2005; Koulakov et al., 2009; Munzarová, Plomerová, Kissling, Vecsey, & Babuška, 2018;
594 Tian & Zhao, 2013). This is generally consistent with what we observe in our study, al-

595 though the differences we detect are perhaps smaller than expected.

596 Several factors can affect the relative performance of seismic tomography with and with-
597 out consideration of anisotropy, including the azimuthal coverage of the events and the
598 characteristics of the anisotropic structure beneath the study area (e.g., Lloyd & van der
599 Lee, 2008; Bezada et al., 2016; Sobolev et al., 1999). Although the backazimuthal dis-
600 tribution of the events used in this study is uneven, our synthetic inversions (Figures S6
601 and S7) exhibit a promising model resolution performance, without much smearing down
602 to 300-400 km, except for eastern Anatolia, where the station density is relatively sparse.
603 Earlier, Bezada et al. (2016) concluded azimuthal coverage would not have a severe impact
604 on anisotropy-related artifacts for teleseismic data. For these reasons it seems unlikely that
605 azimuthal coverage is a dominant factor in the outcome of our inversions. Regarding the
606 spatial character of anisotropy variations, Grésillaud and Cara (1996) revealed that laterally
607 homogeneous anisotropy showing long-wavelength variations over a large study area would
608 not bias isotropic inversions drastically. However, our study region has a long history of sev-
609 eral subduction events and is presently subject to extensional and compressional tectonics
610 as well as an active subducting slab. This tectonic complexity is likely to produce strong
611 lateral variations in anisotropy with relatively short wavelengths, which could reasonably
612 be expected to have a significant impact on teleseismic P-wave traveltime inversions. At
613 the same time, subduction (where the lateral variations in anisotropy have the shortest
614 wavelengths) occupies a relatively small fraction of our entire model space, which may limit
615 the influence of anisotropy on the results. Another important factor is the dip of the fast
616 axes of anisotropy. Sobolev et al. (1999) tested the effect of seismic anisotropy caused by
617 various cases developed under different tectonic conditions. They predicted the highest de-
618 viations to result from isotropic models for the hypothetical scenarios with dipping axes of
619 symmetry (e.g., a 3-5% change in amplitude) and with sub-lithospheric mantle flow (a 2-3%
620 change in amplitude). VanderBeek and Faccenda (2020) in a more recent study have shown
621 that the anisotropic bias in isotropic inversion of teleseismic P-wave delays would not be
622 removed efficiently in cases where azimuthal anisotropy (horizontal fast axes) dominates.
623 The anisotropic inversion of P-wave traveltime residuals can be carried out when the fully
624 anisotropic tensor is approximated to a hexagonal symmetry, where the axis of symmetry
625 is often assumed to be horizontal (e.g., Wei et al., 2019). A recently developed method
626 (Munzarová, Plomerová, & Kissling, 2018) allows for arbitrarily oriented anisotropy in 3D.
627 By applying it to the northern Fennoscandian shield, it was found that the best-fitting

628 fast axes were not always horizontal (Munzarová, Plomerová, Kissling, Vecsey, & Babuška,
629 2018). The numerical model (Confal et al., 2018) employed in estimating the anisotropic
630 contribution to traveltimes delays in this work includes dipping anisotropy above and beneath
631 the active subducting slab, regions where we observed the most significant discrepancies be-
632 tween the isotropic and anisotropy-corrected models.

633 After correcting for the effects of anisotropy, the biggest discrepancies in our models (up to
634 $\pm 2\%$) compared to the isotropic model lie, for instance, in Greece, in the downgoing slab
635 and in central Anatolia. Velocity anomalies in western Greece are up to 2% lower (e.g.,
636 Marker G, Figure 6a/b) and the extent of the low-velocity anomaly parallel to the trench
637 is larger (Marker G, Figure 4b/c). Beneath western Turkey, the low-velocity perturbation
638 inside the slab tear is stronger and shows a different geometry in the anisotropy-corrected
639 model (Marker D, Figures 4b/c, 5b, and 6a/b). This is likely due to the strong anisotropy
640 predicted by the numerical model where mantle flows through the opening in the slab. By
641 correcting for azimuthal anisotropy in central and eastern Anatolia, velocities slightly in-
642 crease (Marker F, Figures 4b/c and 6a/b).

643 By applying anisotropy corrections derived from the numerical model of Confal et al. (2018)
644 we were able to only marginally improve the total variance reduction of the tomography,
645 which can be regarded as an overall measure for the goodness of data fit, by 1.6% (e.g.,
646 an increase from 74.32% to 75.9%, Table 1). Similarly, Eken et al. (2012) reported that
647 applying numerically calculated anisotropic correction terms to the observed data for the
648 Fennoscandian shield would produce an improvement of a few percent in the variance re-
649 duction. Munzarová, Plomerová, Kissling, Vecsey, and Babuška (2018), despite explicitly
650 inverting for anisotropy with an arbitrarily oriented axis of symmetry, obtained only a small
651 improvement of up to 7% for the variance reduction compared to isotropic inversions. Re-
652 sults from completely synthetic tests designed to focus on subduction zones, presented in
653 Bezada et al. (2016), suggest a much better increase in variance reductions should be pos-
654 sible. Counter-intuitively, our synthetic analyses show that isotropic inversions in which
655 anisotropy has (Figure S8b) and has not been accounted for (Figure S8e) yield very similar
656 variance reductions, meaning that even anisotropic traveltimes can be mapped to isotropic
657 velocity variations very successfully. We attribute this mismatch with Bezada et al. (2016)
658 to be primarily due to the fact that our study area is much larger and more complex than
659 the isolated synthetic slab explored in the earlier study. Our model space covers an ac-
660 tive subducting African Plate along the Hellenic and Cyprus trenches and the entirety of

661 Anatolia which experiences present-day extensional and collisional tectonics as well as sub-
662 lithospheric mantle flow evidenced by the azimuthal anisotropy. While lateral changes in
663 the strength and dip of anisotropy have short wavelength changes near trenches, the extend
664 of azimuthal anisotropy is fairly homogeneous over all of Anatolia, which may help explain
665 why there is relatively little bias in the isotropic inversions.

666 Another important factor to consider is our treatment of the shallower velocity and anisotropy
667 structure. The numerical model does not include possible "frozen-in" dipping anisotropy
668 that may be present in the continental lithosphere given the complex deformation history of
669 the area. Regions of high-velocity perturbations in northern Anatolia (Marker 9/IST, Fig-
670 ures 4a, 7c1, and 8) can be related to relatively thick and old lithosphere. Similar anomalies
671 in the study region have also been reported in the early tomography studies of Biryol et al.
672 (2011) and Salaün et al. (2012) and interpreted as the presence of a remnant slab underneath
673 a highly deformed basement of the Pontides and Istanbul Zones, which are characterized
674 by the accretion of continental terrains during the Cimmerian orogeny (Bozkurt, 2001). If
675 any "frozen-in" fabric with a dipping axis of symmetry exists in this region, then ignoring
676 it within our correction procedure will lead to biased inversions (Sobolev et al., 1999) and
677 thus contribute to lowering the total variance reductions with and without corrections. In
678 contrast, Paul et al. (2014) suggested that such complicated anisotropic structures could
679 not be considered for the Aegean-Anatolia, which has a relatively thin mantle lithosphere,
680 given the regionally coherent pattern in the lateral variation of SKS splitting parameter
681 observations. Previously, Plomerová et al. (2011) and Eken et al. (2010) showed that the
682 actual orientation of complicated anisotropic structures beneath the Fennoscandian shield
683 would require a joint inversion of multiple datasets, that is, P-wave traveltime residuals and
684 SKS splitting parameters. Thus, more sophisticated modelling studies are further needed to
685 clarify whether a sub-regional dipping anisotropy is present in this particular region. Crustal
686 anisotropy that can be produced by the layering of sediments, oriented cracks of variable
687 length and width or the foliation of rock complexes (Babuska & Cara, 1991) is neglected in
688 our model since previous studies in the region based on local shear wave splitting measure-
689 ments (e.g., Hurd & Bohnhoff, 2012; Eken et al., 2013; Peng & Ben-Zion, 2005) or receiver
690 function analyses/models (e.g., Licciardi et al., 2018; Vinnik et al., 2016) have indicated
691 its relatively insignificant contribution compared to the predominant mantle anisotropy. If
692 strong and laterally variable crustal anisotropy is present in the study area, it would be an
693 additional source of variance that neither of our models would be able to explain. Addition-

694 ally, although we make efforts to account for isotropic crustal structure, the model we use
695 for this purpose is imperfect. Any potential bias that is introduced by these *a priori* con-
696 straints on the crustal part of the starting model will be identical in both uncorrected and
697 anisotropy-corrected models and equally contribute to the post-inversion variance in both
698 cases. We note that none of these crustal effects were factors considered in the synthetic
699 study of Bezada et al. (2016) which may also help explain why our anisotropic corrections
700 do not achieve the improvement in variance reduction that is suggested by that study.

701
702 Our findings suggest that while upper mantle anisotropy in tectonically active regions such
703 as subduction zones could bias P-wave inversions, the effect is relatively small and comes into
704 play only when interpreting second-order features and the amplitude of specific anomalies.
705 Although these may seem like details in the context of the broader model, they may be
706 important components of the overall interpretation of results, especially if they relate to slab
707 tears and other spatially small features. On the other hand, the fact that changes in the
708 model due to anisotropy are not very significant adds further credibility to the interpretation
709 of the features resolved by this study and previous studies based exclusively on isotropic
710 tomography (e.g., Biryol et al., 2011; Portner et al., 2018).

711 **7 Conclusion**

712 This study contributes to the knowledge of the active tectonic evolution of the Eastern
713 Mediterranean region with a very high-resolution 3D velocity model of the upper mantle as
714 well as to the discussion on the effect of anisotropy on isotropic tomography models. Com-
715 pared to recent isotropic P-wave tomography models, our model benefits from improved
716 station coverage in the western Aegean, and we present new findings, especially about west-
717 ern Greece, the Aegean, and Cyprus. Our tomography results suggest the presence of a
718 horizontal tear in western Greece as part of the northern Hellenic slab segment. A very
719 deep and pronounced vertical tear in western Anatolia, and a sub-horizontal tear between
720 the western and eastern part of the Cyprian slabs can be observed in our results. The
721 Cyprian tear reaches about 200 km depths between the thin eastern and deeper western
722 Cyprian slab. The dip of the slab in the Aegean has flattened from 410 to 660 km depth,
723 while in central Anatolia, the slab appears to not reach deeper than 500 km.
724 Including anisotropy, especially with a significant component of plunging axes of symmetry,
725 in anisotropy-corrected tomography is very challenging, since anisotropy parameters are de-

726 rived from numerical models that are only approximations to true mantle structure. The
727 configuration of these geodynamic numerical models is based on prior first-order interpreta-
728 tions of tomography models themselves. In general, corrected and uncorrected tomographic
729 images indicate similar features that are very robust and can be therefore interpreted with
730 a high degree of certainty, while some smaller features are less stable. Even though the
731 tomography results change weakly by including anisotropy, the changes we see highlight the
732 fact that caution should be taken when using these images to interpret the physical state
733 of the upper mantle or linking them to active tectonics such as volcanism (O'Driscoll et
734 al., 2011) or active subducting slabs (Sobolev et al., 1999). The discrepancies we observe
735 between isotropic and anisotropy-corrected tomography models are similar to those between
736 the results of different tomography studies previously conducted in the region and depend
737 on model parametrization. Our findings show that the influence of anisotropy in the study
738 region should be taken into account, especially when interpreting small-scale features, but
739 that first-order features observed in isotropic models are robust.

740 **Acknowledgments**

741 This is an outcome of an ongoing Ph.D. thesis by Judith M. Confal at the Graduate
742 School of Istanbul Technical University (Turkey) supervised by Tuncay Taymaz. This
743 study is funded by the National Scientific and Technological Research Council of Turkey
744 (TÜBİTAK), project no: ÇAYDAG-115Y248. Furthermore, Judith M. Confal has been
745 awarded a year long scholarship from the German Academic Exchange Service (DAAD,
746 Jahresstipendien für Doktorandinnen und Doktoranden Studienjahr 2017/18) with the refer-
747 ence number 91671753. We are thankful to the University of Minnesota, Minneapolis, USA,
748 for supporting the research, with the permission for the use of their servers and a study visit.
749 We thank the Turkish Academy of Sciences (TÜBA) in the framework for Young Scientist
750 Award Program (TÜBA-GEBİP) and the Alexander von Humboldt Foundation Research
751 Fellowship Award for financial support and for further providing computing facilities and
752 other relevant resources through Humboldt-Stiftung Follow-Up Programme.

753 The IRIS Data Management Center (<https://www.iris.edu/hq/>) was used to access seismic
754 waveforms and the United States Geological Survey (USGS) to obtain earthquake hypocen-
755 tral details respectively. This work includes data from various permanent and temporary
756 regional networks (KO-Kandilli Observatory-KOERI (<https://doi.org/10.7914/SN/KO>),
757 HT-Aristotle University of Thessaloniki Seismological Network-NOA (<https://doi.org/10.7914/SN/HT>),

758 6G-KOERI (https://doi.org/10.7914/SN/6G_2013), Z3-EGELADOS Network (<https://doi.org/10.14470/M87550267382>), YL-IRISDMC (https://doi.org/10.7914/SN/YL_2005),
759
760 6E-GEOFON, TU-National Seismic Network of Turkey (DDA) (https://doi.org/10.7914/SN/3G_2007),
761 HL-Hellenic Seismic Network-NOA (<https://doi.org/10.7914/SN/HL>), IU-IRIS/USGS
762 (<https://doi.org/10.7914/SN/IU>), GE-GEOFON (<https://doi.org/10.14470/TR560404>),
763 XG-IRISDMC (https://doi.org/10.7914/SN/XG_1999), XH-IRISDMC (https://doi.org/10.7914/SN/XH_2002),
764 XY-RESIF (<https://doi.org/10.15778/RESIF.XY2007>), HP-University of Patras (<https://doi.org/10.7914/SN/HP>), Seismological Laboratory (PSLNET)-NOA, YH-IRISDMC (https://doi.org/10.7914/SN/YH_2012), MN-Mediterranean Very Broadband Seismographic Network-
765
766 INGV (<https://doi.org/10.13127/SD/fBBBtDtd6q>), HA-National and Kapodistrian Uni-
767
768 versity of Athens (<https://doi.org/10.7914/SN/HA>), Seismological Laboratory (NKUA)-
769
770 NOA, ZZ-GEOFON (<https://doi.org/10.14470/MM7557265463>), XW-RESIF (<https://doi.org/10.15778/RESIF.XW2007>)) mostly operated by the Kandilli Observatory and
771
772 Earthquake Research Institute-Regional Earthquake-Tsunamic Monitoring Center (KOERI-
773
774 RETMC) and National Seismic Network (DDA) the Greek National Observatory of Athens
775
776 (NOA-IG). Temporal deployments like FaultLab from the CD-CAT experiment (https://doi.org/10.7914/SN/YB_2013) improved the station coverage and are available from the
777
778 IRIS Data Management Center as well. Digital waveform recordings were retrieved from
779
780 EIDA, an initiative within ORFEUS (<http://www.orfeus-eu.org/data/eida/networks/>).
781
782 Data from prior SKS splitting measurements were taken from Wüstefeld and Bokelmann
783
784 (2007). The figures are made using the Generic Mapping Tools (Wessel & Smith, 1998),
785
786 GeoMapApp (<http://www.geomapapp.org>), Matlab and Inkscape softwares. The tomog-
787
788 raphy results can be downloaded on OSF under a project with the same title as this paper
789
790 (<https://osf.io/bu46n/>). We would like to thank the Editor Martha Savage, Associate
791
792 Editor Sebastien Chevrot, Anne Paul and an anonymous reviewer. Their constructive ad-
793
794 vice, suggestions, and judicial reviews improved this study immensely. We gratefully thank
795
796 Caroline Johnson for reviewing an earlier version of the manuscript.

785 References

- 786 Amaru, M. (2007). *Global travel time tomography with 3-D reference models* (Vol. 274).
787 Utrecht University.
- 788 Babuska, V., & Cara, M. (1991). *Seismic anisotropy in the Earth* (Vol. 10). Springer Science
789 & Business Media.

- 790 Bezada, M., Faccenda, M., & Toomey, D. (2016). Representing anisotropic subduction zones
791 with isotropic velocity models: A characterization of the problem and some steps on
792 a possible path forward. *Geochemistry, Geophysics, Geosystems*, *17*(8), 3164–3189.
- 793 Bezada, M., Humphreys, E., Toomey, D., Harnafi, M., Dávila, J., & Gallart, J. (2013).
794 Evidence for slab rollback in westernmost mediterranean from improved upper mantle
795 imaging. *Earth Planet. Sci. Lett.*, *368*, 51–60.
- 796 Biryol, C. B., Beck, S. L., Zandt, G., & Özacar, A. A. (2011). Segmented African litho-
797 sphere beneath the Anatolian region inferred from teleseismic P-wave tomography.
798 *Geophysical Journal International*, *184*(3), 1037–1057.
- 799 Biryol, C. B., Zandt, G., Beck, S. L., Ozacar, A. A., Adiyaman, H. E., & Gans, C. R. (2010).
800 Shear wave splitting along a nascent plate boundary: the North Anatolian Fault Zone.
801 *Geophysical Journal International*, *181*(3), 1201–1213.
- 802 Blom, N., Gokhberg, A., & Fichtner, A. (2020). Seismic waveform tomography of the central
803 and eastern Mediterranean upper mantle. *Solid Earth*, *11*(2), 669–690.
- 804 Bozkurt, E. (2001). Neotectonics of Turkey—a synthesis. *Geodinamica acta*, *14*(1-3), 3–30.
- 805 Browaeys, J. T., & Chevrot, S. (2004). Decomposition of the elastic tensor and geophysical
806 applications. *Geophysical Journal International*, *159*(2), 667–678.
- 807 Confal, J. M., Eken, T., Tilmann, F., Yolsal-Çevikbilen, S., Çubuk-Sabuncu, Y., Saygin,
808 E., & Taymaz, T. (2016). Investigation of mantle kinematics beneath the Hellenic-
809 subduction zone with teleseismic direct shear waves. *Physics of the Earth and Plane-
810 tary Interiors*, *261*, 141–151.
- 811 Confal, J. M., Faccenda, M., Eken, T., & Taymaz, T. (2018). Numerical simulation of
812 3-D mantle flow evolution in subduction zone environments in relation to seismic
813 anisotropy beneath the eastern Mediterranean region. *Earth and Planetary Science
814 Letters*, *497*, 50–61.
- 815 Cosentino, D., Schildgen, T. F., Cipollari, P., Faranda, C., Gliozzi, E., Hudáčková, N., . . .
816 Strecker, M. R. (2012). Late Miocene surface uplift of the southern margin of the
817 Central Anatolian Plateau, Central Taurides, Turkey. *Bulletin*, *124*(1-2), 133–145.
- 818 Çubuk-Sabuncu, Y., Taymaz, T., & Fichtner, A. (2017). 3-D crustal velocity structure of
819 western Turkey: Constraints from full-waveform tomography. *Physics of the Earth
820 and Planetary Interiors*, *270*, 90–112.
- 821 Delph, J. R., Abgarmi, B., Ward, K. M., Beck, S. L., Özacar, A. A., Zandt, G., . . . Kalafat,
822 D. (2017). The effects of subduction termination on the continental lithosphere:

- 823 Linking volcanism, deformation, surface uplift, and slab tearing in central Anatolia.
824 *Geosphere*, 13(6), 1788–1805.
- 825 Delph, J. R., Biryol, C. B., Beck, S. L., Zandt, G., & Ward, K. M. (2015). Shear wave
826 velocity structure of the Anatolian Plate: anomalously slow crust in southwestern
827 Turkey. *Geophysical Journal International*, 202(1), 261–276.
- 828 Eakin, C. M., Obrebski, M., Allen, R. M., Boyarko, D. C., Brudzinski, M. R., & Porritt,
829 R. (2010). Seismic anisotropy beneath Cascadia and the Mendocino triple junction:
830 Interaction of the subducting slab with mantle flow. *Earth and Planetary Science
831 Letters*, 297(3-4), 627–632.
- 832 Eberhart-Phillips, D., & Reyners, M. (2009). Three-dimensional distribution of seismic
833 anisotropy in the Hikurangi subduction zone beneath the central North Island, New
834 Zealand. *Journal of Geophysical Research: Solid Earth*, 114(B6).
- 835 Eken, T., Bohnhoff, M., Bulut, F., Can, B., & Aktar, M. (2013). Crustal Anisotropy in
836 the Eastern Sea of Marmara Region in Northwestern Turkey Crustal Anisotropy in the
837 Eastern Sea of Marmara Region in Northwestern Turkey. *Bulletin of the Seismological
838 Society of America*, 103(2A), 911–924.
- 839 Eken, T., Plomerová, J., Roberts, R., Vecsey, L., Babuška, V., Shomali, H., & Bodvarsson,
840 R. (2010). Seismic anisotropy of the mantle lithosphere beneath the Swedish National
841 Seismological Network (SNSN). *Tectonophysics*, 480(1-4), 241–258.
- 842 Eken, T., Plomerová, J., Vecsey, L., Babuška, V., Roberts, R., Shomali, H., & Bodvarsson,
843 R. (2012). Effects of seismic anisotropy on P-velocity tomography of the Baltic Shield.
844 *Geophysical Journal International*, 188(2), 600–612.
- 845 Evangelidis, C. (2017). Seismic anisotropy in the Hellenic subduction zone: Effects of slab
846 segmentation and subslab mantle flow. *Earth and Planetary Science Letters*, 480,
847 97–106.
- 848 Evangelidis, C., Liang, W.-T., Melis, N., & Konstantinou, K. (2011). Shear wave anisotropy
849 beneath the Aegean inferred from SKS splitting observations. *Journal of Geophysical
850 Research: Solid Earth (1978–2012)*, 116(B4314).
- 851 Faccenda, M. (2014). Mid mantle seismic anisotropy around subduction zones. *Physics of
852 the Earth and Planetary Interiors*, 227, 1–19.
- 853 Faccenda, M., & Capitanio, F. (2013). Seismic anisotropy around subduction zones: In-
854 sights from three-dimensional modeling of upper mantle deformation and SKS splitting
855 calculations. *Geochemistry, Geophysics, Geosystems*, 14(1), 243–262.

- 856 Feld, C., Mechie, J., Huebscher, C., Hall, J., Nicolaidis, S., Gurbuz, C., ... Weber, M.
857 (2017). Crustal structure of the Eratosthenes Seamount, Cyprus and S. Turkey from
858 an amphibian wide-angle seismic profile. *Tectonophysics*, 700, 32–59.
- 859 Fichtner, A., Saygin, E., Taymaz, T., Cupillard, P., Capdeville, Y., & Trampert, J. (2013).
860 The deep structure of the North Anatolian fault zone. *Earth and Planetary Science
861 Letters*, 373, 109–117.
- 862 Fichtner, A., Trampert, J., Cupillard, P., Saygin, E., Taymaz, T., Capdeville, Y., & Vil-
863 laseñor, A. (2013). Multiscale full waveform inversion. *Geophysical Journal Interna-
864 tional*, 194(1), 534–556.
- 865 Görür, N. (1988). Timing of opening of the Black Sea basin. *Tectonophysics*, 147(3-4),
866 247–262.
- 867 Govers, R., & Fichtner, A. (2016). Signature of slab fragmentation beneath Anatolia from
868 full-waveform tomography. *Earth and Planetary Science Letters*, 450, 10–19.
- 869 Grésillaud, A., & Cara, M. (1996). Anisotropy and P-wave tomography: a new approach
870 for inverting teleseismic data from a dense array of stations. *Geophysical Journal
871 International*, 126(1), 77–91.
- 872 Guillaume, B., Husson, L., Funicello, F., & Faccenna, C. (2013). The dynamics of laterally
873 variable subductions: laboratory models applied to the Hellenides. *Solid Earth*, 4,
874 179–200.
- 875 Gürer, D., Plunder, A., Kirst, F., Corfu, F., Schmid, S. M., & van Hinsbergen, D. J.
876 (2018). A long-lived Late Cretaceous–early Eocene extensional province in Anatolia?
877 Structural evidence from the Ivriz Detachment, southern central Turkey. *Earth and
878 Planetary Science Letters*, 481, 111–124.
- 879 Handy, M. R., Giese, J., Schmid, S. M., Pleuger, J., Spakman, W., Onuzi, K., & Ustaszewski,
880 K. (2019). Coupled crust-mantle response to slab tearing, bending and rollback along
881 the Dinaride-Hellenide orogen. *Tectonics*.
- 882 Hansen, S. E., Evangelidis, C. P., & Papadopoulos, G. A. (2019). Imaging Slab Detachment
883 Within the Western Hellenic Subduction Zone. *Geochemistry, Geophysics, Geosys-
884 tems*, 20(2), 895–912.
- 885 Hurd, O., & Bohnhoff, M. (2012). Stress-and Structure-Induced Shear-Wave Anisotropy
886 along the 1999 Izmit Rupture, Northwest Turkey. *Bulletin of the Seismological Society
887 of America*, 102(5), 2177–2188.
- 888 Ishise, M., & Oda, H. (2005). Three-dimensional structure of P-wave anisotropy beneath

- 889 the Tohoku district, northeast Japan. *Journal of Geophysical Research: Solid Earth*,
890 *110*(B7).
- 891 Jolivet, L. (2001). A comparison of geodetic and finite strain pattern in the Aegean,
892 geodynamic implications. *Earth and Planetary Science Letters*, *187*(1), 95–104.
- 893 Jolivet, L., & Faccenna, C. (2000). Mediterranean extension and the Africa-Eurasia collision.
894 *Tectonics*, *19*(6), 1095–1106.
- 895 Jolivet, L., Faccenna, C., Huet, B., Labrousse, L., Le Pourhiet, L., Lacombe, O., ... oth-
896 ers (2013). Aegean tectonics: Strain localisation, slab tearing and trench retreat.
897 *Tectonophysics*, *597*, 1–33.
- 898 Jolivet, L., Menant, A., Clerc, C., Sternai, P., Bellahsen, N., Leroy, S., ... Gorini, C. (2018).
899 Extensional crustal tectonics and crust-mantle coupling, a view from the geological
900 record. *Earth-Science Reviews*, *185*, 1187–1209.
- 901 Jolivet, L., Menant, A., Sternai, P., Rabillard, A., Arbaret, L., Augier, R., ... others (2015).
902 The geological signature of a slab tear below the Aegean. *Tectonophysics*, *659*, 166–
903 182.
- 904 Kaminski, E., Ribe, N. M., & Browaeys, J. T. (2004). D-Rex, a program for calculation of
905 seismic anisotropy due to crystal lattice preferred orientation in the convective upper
906 mantle. *Geophysical Journal International*, *158*(2), 744–752.
- 907 Karabulut, H., Paul, A., Özbakır, A. D., Ergün, T., & Şentürk, S. (2019). A new crustal
908 model of the anatolia–aegean domain: evidence for the dominant role of isostasy in the
909 support of the anatolian plateau. *Geophysical Journal International*, *218*(1), 57–73.
- 910 Kennett, B., Engdahl, E., & Buland, R. (1995). Constraints on seismic velocities in the
911 Earth from traveltimes. *Geophysical Journal International*, *122*(1), 108–124.
- 912 Keskin, M. (2003). Magma generation by slab steepening and breakoff beneath a subduction-
913 accretion complex: An alternative model for collision-related volcanism in Eastern
914 Anatolia, Turkey. *Geophysical Research Letters*, *30*(24).
- 915 Kind, R., Eken, T., Tilmann, F., Sodoudi, F., Taymaz, T., Bulut, F., ... Schneider, F.
916 (2015). Thickness of the lithosphere beneath Turkey and surroundings from S-receiver
917 functions. *Solid Earth*, *6*(3), 971.
- 918 Koulakov, I., Jakovlev, A., & Luehr, B. G. (2009). Anisotropic structure beneath cen-
919 tral Java from local earthquake tomography. *Geochemistry, Geophysics, Geosystems*,
920 *10*(2).
- 921 Le Pichon, X., & Kreemer, C. (2010). The Miocene-to-present kinematic evolution of the

- 922 eastern Mediterranean and Middle East and its implications for dynamics. *Annual*
923 *Review of Earth and Planetary Sciences*, *38*, 323–351.
- 924 Licciardi, A., Eken, T., Taymaz, T., Agostinetti, N. P., & Yolsal-Çevikbilen, S. (2018).
925 Seismic anisotropy in central North Anatolian Fault Zone and its implications on
926 crustal deformation. *Physics of the Earth and Planetary Interiors*, *277*, 99–112.
- 927 Lloyd, S., & van der Lee, S. (2008). Influence of observed mantle anisotropy on isotropic
928 tomographic models. *Geochemistry, Geophysics, Geosystems*, *9*(7).
- 929 Ma, J., Tian, Y., Zhao, D., Liu, C., & Liu, T. (2019). Mantle Dynamics of Western Pacific
930 and East Asia: New Insights from P Wave Anisotropic Tomography. *Geochemistry,*
931 *Geophysics, Geosystems*, *20*(7), 3628–3658.
- 932 McClusky, S., Balassanian, S., Barka, A., Demir, C., Ergintav, S., Georgiev, I., ... others
933 (2000). Global Positioning System constraints on plate kinematics and dynamics in the
934 eastern Mediterranean and Caucasus. *Journal of Geophysical Research: Solid Earth*,
935 *105*(B3), 5695–5719.
- 936 Munzarová, H., Plomerová, J., & Kissling, E. (2018). Novel anisotropic teleseismic body-
937 wave tomography code AniTomo to illuminate heterogeneous anisotropic upper man-
938 tle: Part I Theory and inversion tuning with realistic synthetic data. *Geophysical*
939 *Journal International*, *215*(1), 524–545.
- 940 Munzarová, H., Plomerová, J., Kissling, E., Vecsey, L., & Babuška, V. (2018). Novel
941 anisotropic teleseismic body-wave tomography code AniTomo to illuminate hetero-
942 geneous anisotropic upper mantle: Part II—Application to data of passive seismic
943 experiment LAPNET in northern Fennoscandia. *Geophysical Journal International*,
944 *215*(2), 1388–1409.
- 945 Mutlu, A. K., & Karabulut, H. (2011). Anisotropic Pn tomography of Turkey and adjacent
946 regions. *Geophysical Journal International*, *187*(3), 1743–1758.
- 947 O’Driscoll, L. J., Humphreys, E. D., & Schmandt, B. (2011). Time corrections to teleseismic
948 P delays derived from SKS splitting parameters and implications for western US P-
949 wave tomography. *Geophysical Research Letters*, *38*(19).
- 950 Okay, A. I., & Tüysüz, O. (1999). Tethyan sutures of northern Turkey. *Geological Society,*
951 *London, Special Publications*, *156*(1), 475–515.
- 952 Olive, J.-A., Pearce, F., Rondenay, S., & Behn, M. D. (2014). Pronounced zonation of seismic
953 anisotropy in the Western Hellenic subduction zone and its geodynamic significance.
954 *Earth and Planetary Science Letters*, *391*, 100–109.

- 955 Özbakır, A. D., Govers, R., & Fichtner, A. (2020). The Kefalonia Transform Fault: A
 956 STEP fault in the making. *Tectonophysics*, 228471.
- 957 Paul, A., Karabulut, H., Mutlu, A. K., & Salaün, G. (2014). A comprehensive and densely
 958 sampled map of shear-wave azimuthal anisotropy in the Aegean–Anatolia region. *Earth
 959 and Planetary Science Letters*, 389, 14–22.
- 960 Pearce, F. D., Rondenay, S., Sachpazi, M., Charalampakis, M., & Royden, L. H. (2012).
 961 Seismic investigation of the transition from continental to oceanic subduction along
 962 the western Hellenic Subduction Zone. *Journal of Geophysical Research: Solid Earth
 963 (1978–2012)*, 117(B7).
- 964 Peng, Z., & Ben-Zion, Y. (2005). Spatiotemporal variations of crustal anisotropy from simi-
 965 lar events in aftershocks of the 1999 M 7.4 Izmit and M 7.1 Düzce, Turkey, earthquake
 966 sequences. *Geophysical Journal International*, 160(3), 1027–1043.
- 967 Piromallo, C., & Morelli, A. (2003). P wave tomography of the mantle under the Alpine-
 968 Mediterranean area. *Journal of Geophysical Research: Solid Earth (1978–2012)*,
 969 108(B2). (2065)
- 970 Plomerová, J., Vecsey, L., Babuška, V., et al. (2011). Domains of archean mantle litho-
 971 sphere deciphered by seismic anisotropy inferences from the lapnet array in northern
 972 fennoscandia. *Solid Earth*, 2(2), 303–313.
- 973 Portner, D. E., Delph, J. R., Biryol, C. B., Beck, S. L., Zandt, G., Özacar, A. A., ...
 974 Türkelli, N. (2018). Subduction termination through progressive slab deformation
 975 across Eastern Mediterranean subduction zones from updated P-wave tomography
 976 beneath Anatolia. *Geosphere*, 14(3), 907–925.
- 977 Reilinger, R., McClusky, S., Vernant, P., Lawrence, S., Ergintav, S., Cakmak, R., ... others
 978 (2006). GPS constraints on continental deformation in the Africa-Arabia-Eurasia con-
 979 tinental collision zone and implications for the dynamics of plate interactions. *Journal
 980 of Geophysical Research: Solid Earth*, 111(B5). (B05411)
- 981 Roche, V., Bouchot, V., Beccaletto, L., Jolivet, L., Guillou-Frottier, L., Tuduri, J., ...
 982 Tokay, B. (2019). Structural, lithological, and geodynamic controls on geothermal ac-
 983 tivity in the Menderes geothermal Province (Western Anatolia, Turkey). *International
 984 Journal of Earth Sciences*, 108(1), 301–328.
- 985 Salaün, G., Pedersen, H. A., Paul, A., Farra, V., Karabulut, H., Hatzfeld, D., ... others
 986 (2012). High-resolution surface wave tomography beneath the Aegean-Anatolia region:
 987 constraints on upper-mantle structure. *Geophysical Journal International*, 190(1),

- 988 406–420.
- 989 Sandvol, E. (2013). Continental Dynamics/Central Anatolian Tectonics: Surface to mantle
990 dynamics during collision to escape. International Federation of Digital Seismograph
991 Networks. Dataset/Seismic Network. 10.7914/SN/YB.2013.
- 992 Sandvol, E., Turkelli, N., Zor, E., Gok, R., Bekler, T., Gurbuz, C., ... Barazangi, M.
993 (2003). Shear wave splitting in a young continent-continent collision: An example
994 from eastern Turkey. *Geophysical Research Letters*, *30*(24).
- 995 Saunders, P., Priestley, K., & Taymaz, T. (1998). Variations in the crustal structure beneath
996 western Turkey. *Geophysical Journal International*, *134*(2), 373–389.
- 997 Schattner, U. (2010). What triggered the early-to-mid Pleistocene tectonic transition across
998 the entire eastern Mediterranean? *Earth and Planetary Science Letters*, *289*(3-4),
999 539–548.
- 1000 Schiffer, C., Eken, T., Rondenay, S., & Taymaz, T. (2019). Localized crustal deformation
1001 along the central North Anatolian Fault Zone revealed by joint inversion of P-receiver
1002 functions and P-wave polarizations. *Geophysical Journal International*, *217*(1), 682–
1003 702.
- 1004 Schildgen, T. F., Yildirim, C., Cosentino, D., & Strecker, M. R. (2014). Linking slab break-
1005 off, Hellenic trench retreat, and uplift of the Central and Eastern Anatolian plateaus.
1006 *Earth-Science Reviews*, *128*, 147–168.
- 1007 Schmandt, B., & Humphreys, E. (2010). Seismic heterogeneity and small-scale convection in
1008 the southern California upper mantle. *Geochemistry, Geophysics, Geosystems*, *11*(5).
- 1009 Sobolev, S. V., Grésillaud, A., & Cara, M. (1999). How robust is isotropic delay time
1010 tomography for anisotropic mantle? *Geophysical research letters*, *26*(4), 509–512.
- 1011 Tan, O., & Taymaz, T. (2006). Active tectonics of the Caucasus: Earthquake source mech-
1012 anisms and rupture histories obtained from inversion of teleseismic body waveforms.
1013 *SPECIAL PAPERS-GEOLOGICAL SOCIETY OF AMERICA*, *409*, 531.
- 1014 Taymaz, T. (1996). S-P-wave travelttime residuals from earthquakes and lateral inhomog-
1015 eneity in the upper mantle beneath the Aegean and the Hellenic Trench near Crete.
1016 *Geophysical Journal International*, *127*(2), 545–558.
- 1017 Taymaz, T., Westaway, R., & Reilinger, R. (2004). Active faulting and crustal deformation
1018 in the Eastern Mediterranean region. *Tectonophysics*, *391*(1), 1–9.
- 1019 Taymaz, T., Yilmaz, Y., & Dilek, Y. (2007). The geodynamics of the Aegean and Anatolia:
1020 introduction. *Geological Society, London, Special Publications*, *291*(1), 1–16.

- 1021 Tian, Y., & Zhao, D. (2013). Reactivation and mantle dynamics of North China Craton: in-
1022 sight from P-wave anisotropy tomography. *Geophysical Journal International*, *195*(3),
1023 1796–1810.
- 1024 Timkó, M., Kovács, I., & Wéber, Z. (2019). 3D P-wave velocity image beneath the Pan-
1025 nonian Basin using travelttime tomography. *Acta Geodaetica et Geophysica*, *54*(3),
1026 373–386.
- 1027 Tirel, C., Gueydan, F., Tiberi, C., & Brun, J.-P. (2004). Aegean crustal thickness inferred
1028 from gravity inversion. Geodynamical implications. *Earth and Planetary Science Let-*
1029 *ters*, *228*(3-4), 267–280.
- 1030 Toomey, D. R., Solomon, S. C., & Purdy, G. (1994). Tomographic imaging of the shallow
1031 crustal structure of the East Pacific Rise at 9 30 N. *Journal of Geophysical Research:*
1032 *Solid Earth*, *99*(B12), 24135–24157.
- 1033 Vanacore, E., Taymaz, T., & Saygin, E. (2013). Moho structure of the Anatolian Plate
1034 from receiver function analysis. *Geophysical Journal International*, *193*(1), 329–337.
- 1035 VanDecar, J., & Crosson, R. (1990). Determination of teleseismic relative phase arrival times
1036 using multi-channel cross-correlation and least squares. *Bulletin of the Seismological*
1037 *Society of America*, *80*(1), 150–169.
- 1038 VanderBeek, B. P., & Faccenda, M. (2020). Can Teleseismic Travel-Times Constrain 3D
1039 Anisotropic Structure in Subduction Zones? Insights from Realistic Synthetic Exper-
1040 iments. In *EGU General Assembly Conference Abstracts* (Vol. 22, p. 14886). doi:
1041 <https://doi.org/10.5194/egusphere-egu2020-14886>
- 1042 Vinnik, L., Oreshin, S., & Erduran, M. (2016). Melt in the mantle and seismic azimuthal
1043 anisotropy: evidence from Anatolia. *Geophysical Supplements to the Monthly Notices*
1044 *of the Royal Astronomical Society*, *205*(1), 523–530.
- 1045 Wang, J., & Zhao, D. (2013). P-wave tomography for 3-D radial and azimuthal anisotropy
1046 of Tohoku and Kyushu subduction zones. *Geophysical Journal International*, *193*(3),
1047 1166–1181.
- 1048 Wei, W., Zhao, D., Wei, F., Bai, X., & Xu, J. (2019). Mantle dynamics of the Eastern
1049 Mediterranean and Middle East: Constraints from P-wave anisotropic tomography.
1050 *Geochemistry, Geophysics, Geosystems*.
- 1051 Wessel, P., & Smith, W. H. (1998). New, improved version of Generic Mapping Tools
1052 released. *Eos, Transactions American Geophysical Union*, *79*(47), 579–579.
- 1053 Wortel, M., & Spakman, W. (2000). Subduction and slab detachment in the Mediterranean-

- 1054 Carpathian region. *Science*, 290(5498), 1910–1917.
- 1055 Wüstefeld, A., & Bokermann, G. (2007). Null detection in shear-wave splitting measure-
1056 ments. *Bulletin of the Seismological Society of America*, 97(4), 1204–1211.
- 1057 Yolsal-Çevikbilen, S. (2014). Seismic anisotropy along the Cyprean arc and northeast
1058 Mediterranean Sea inferred from shear wave splitting analysis. *Physics of the Earth
1059 and Planetary Interiors*, 233, 112–134.
- 1060 You, T., & Zhao, D. (2012). Seismic anisotropy and heterogeneity in the Alaska subduction
1061 zone. *Geophysical Journal International*, 190(1), 629–649.